

AN ABSTRACT OF THESIS OF

Jennifer Lyons for the degree of Master of Science in Nuclear Engineering presented on July 31, 2013.

Title: Reactor Physics Model of the Advanced Test Reactor using TRIGA[®] Fuel through Application of Serpent 2

Abstract approved: _____

Wade R. Marcum

The Advanced Test Reactor (ATR), under the Reduced Enrichment for Research and Test Reactors (RERTR) Program and the Global Threat Reduction Initiative (GTRI), is conducting feasibility studies for the conversion of its fuel from a highly enriched uranium (HEU) composition to a low enriched uranium (LEU) composition. These studies have considered a wide variety of LEU plate-type fuels to replace the current HEU fuel. Continuing to investigate potential alternatives to the present HEU fuel form, this study presents a preliminary analysis of TRIGA[®] fuel within the current ATR fuel envelopes and compares it to the functional requirements delineated by the Naval Reactors Program, which includes: greater than $4.8E+14$ fissions/s/g of ^{235}U , a fast to thermal neutron flux ratio that is less than 5% deviation of its current value, a constant cycle power within the corner lobes, and an operational cycle length of 56 days at 120 MW. Other parameters outside those put forth by the Naval Reactors Program which are investigated herein include axial and radial power profiles, effective delayed neutron fraction, and mean neutron generation time.

© Copyright by Jennifer Lyons
July 31, 2013
All Rights Reserved

Reactor Physics Model of the Advanced Test Reactor using TRIGA[®] Fuel through
Application of Serpent 2

by
Jennifer Lyons

A THESIS
Submitted to
Oregon State University

in partial fulfillment of
the requirements for the
degree of
Master of Science

Presented July 31, 2013
Commencement June 2014

Master of Science thesis of Jennifer Lyons presented on July 31, 2013.

APPROVED:

Major Professor, representing Nuclear Engineering

Head of the Department of Nuclear Engineering and Radiation Health Physics

Dean of the Graduate School

I understand that my thesis will become part of the permanent collection of Oregon State University libraries. My signature below authorizes release of my thesis to any reader upon request.

Jennifer Lyons, Author

ACKNOWLEDGEMENTS

I would like to thank my friends, family, colleagues, and advisors for their support, most notably Dr. Wade Marcum, Dr. Mark DeHart, and Sean Morrell.

I would also like to thank Idaho National Laboratory and the Global Threat Reduction Initiative for funding this work.

TABLE OF CONTENTS

	<u>Page</u>
1 INTRODUCTION.....	1
1.1 Motivation.....	2
1.2 Objective.....	3
1.3 Document Overview.....	5
2 SURVEY OF LITERATURE.....	6
2.1 Computational Reactor Physics Tools.....	6
2.1.1 Deterministic Computational Tools.....	7
2.1.2 Stochastic Computational Tools.....	7
2.1.3 Depletion Methodology.....	9
2.1.4 Computational Tools Closing.....	10
2.2 Core Fuel Development and Qualification.....	11
2.2.1 Research Reactors.....	11
2.2.2 The Advanced Test Reactor Conversion.....	12
3 ADVANCED TEST REACTOR OVERVIEW.....	13
4 MODELS AND METHODOLOGY.....	16
4.1 Baseline Model.....	16
4.2 TRIGA [®] Fuel.....	17
4.3 TRIGA [®] Fuel Models.....	20
4.3.1 Model 1.....	20
4.3.2 Model 2.....	21
4.3.3 Model 3.....	23
4.3.4 Model 4.....	24
4.3.5 Model 5.....	25
4.3.6 Model 6.....	26
4.4 Reactor Characterization.....	27

TABLE OF CONTENTS (Continued)

	<u>Page</u>
4.4.1 Depletion Analysis	27
4.4.2 OSCC Analysis.....	27
4.4.3 Specific Fission Rate of ²³⁵ U	28
4.4.4 Neutron Flux Analysis.....	30
4.4.5 Corner Lobe Power.....	31
4.4.6 Further Model Characterization	31
5 RESULTS AND DISCUSSION	32
5.1 Depletion Analysis	32
5.2 OSCC Analysis.....	33
5.3 Specific Fission Rate of ²³⁵ U	36
5.4 Neutron Flux Analysis.....	37
5.5 Corner Lobe Power.....	44
5.6 Further Model Characterization	45
5.6.1 Model 1 Pin Power Analysis	45
5.6.2 Effective Delayed Neutron Fraction & Mean Neutron Generation Time	48
6 CONCLUSIONS	51
6.1 Concluding Remarks	51
6.2 Future Work.....	52
7 BIBLIOGRAPHY	54
8 NOMENCLATURE.....	59
9 APPENDIX A: SENSITIVITY STUDY ON H/ZR RATIO	62
10 APPENDIX B: OTHER TRIGA [®] COMPOSITIONS	64
10.1 30/20 TRIGA [®] Fuel.....	64
10.2 45/20 TRIGA [®] Fuel.....	67

TABLE OF CONTENTS (Continued)

	<u>Page</u>
10.3 40/20 TRIGA [®] Fuel.....	70
11 APPENDIX C: VARIED BURN REGIONS.....	71
12 APPENDIX D: TABULATED VALUES, STATISTICAL ERROR, AND ERROR ANALYSIS.....	73
12.1 Depletion Values and Percent Error.....	73
12.2 OSCC Analysis Error Analysis.....	73
12.3 Specific Fission Rate Error Analysis.....	74
12.4 Neutron Flux Analysis Values and % Error.....	75
12.5 Corner Lobe Power Error Analysis.....	77
12.6 Pin Power Values and Percent Error.....	78
12.7 Effective Delayed Neutron Fraction and Mean Neutron Generation Time	80

LIST OF FIGURES

<u>Figure</u>	<u>Page</u>
Figure 3.1: Advanced Test Reactor core cross section.....	14
Figure 3.2: Pictorial view of ATR fuel element.....	15
Figure 4.1: HEU ATR model.....	17
Figure 4.2: Sketch of a top-down view of Model 1.....	21
Figure 4.3: Top-down view of Model 2.....	22
Figure 4.4: Top-down view of Model 3.....	23
Figure 4.5: Top-down view of Model 4.....	24
Figure 4.6: Top-down view of Model 5.....	25
Figure 4.7: Top-down view of Model 6.....	26
Figure 4.8: The SW IPT with the experiment cylinder.....	29
Figure 5.1: Depletion calculation of the HEU 94CIC and TRIGA [®] Model 1.....	33
Figure 5.2: Reactivity vs. OSCC Rotation for 35/20 TRIGA fuel.....	34
Figure 5.3: OSCC Rotation vs. MWd for 35/20 TRIGA fuel.....	35
Figure 5.4: NW trap flux spectrum (per unit lethargy).....	40
Figure 5.5: SW trap flux spectrum (per unit lethargy).....	40
Figure 5.6: NE trap flux spectrum (per unit lethargy).....	41
Figure 5.7: SE trap flux spectrum (per unit lethargy).....	41
Figure 5.8: Center flux spectrum (per unit lethargy).....	42
Figure 5.9: West flux trap flux spectrum (per unit lethargy).....	42
Figure 5.10: East flux trap flux spectrum (per unit lethargy).....	43
Figure 5.11: North flux trap flux spectrum (per unit lethargy).....	43
Figure 5.12: South flux trap flux spectrum (per unit lethargy).....	44
Figure 5.13: Lobe powers over one 56-day cycle.....	45
Figure 5.14: Power per rod for elements 1-5 for Model 1.....	46
Figure 5.15: Axial power profile for the hottest rod, rod 16 in element 1.....	47
Figure 5.16: Radial power profile for the hottest rod, rod 16 in element 1.....	48
Figure 5.17: Effective delayed neutron fraction over one cycle.....	49
Figure 5.18: Mean neutron generation time over one cycle.....	49
Figure 9.1: The effects of the H/Zr ratio over one 56-day, 120 MW cycle.....	63

LIST OF FIGURES (Continued)

<u>Figure</u>	<u>Page</u>
Figure 10.1: Reactivity vs. OSCC rotation angle for the 30/20 TRIGA fuel.....	65
Figure 10.2: Burnup for the 30/20 loaded Model 1 and the HEU model.....	66
Figure 10.3: OSCC rotation vs. MWd for Model 1 fueled with 30/20 TRIGA fuel....	67
Figure 10.4: Reactivity vs. OSCC rotation with Incoloy and stainless steel cladding.	68
Figure 10.5: Burnup for the 45/20 TRIGA fuel	69
Figure 10.6: OSCC rotation vs. MWd for the 45/20 TRIGA fuel.....	70
Figure 11.1: The varied burn regions for the TRIGA [®] fuel	72

LIST OF TABLES

<u>Table</u>	<u>Page</u>
Table 4.1: Variables for TRIGA [®] fuel rod composition [36,37].....	18
Table 4.2: TRIGA fuel rod compositions.....	20
Table 4.3: Specific fission rate experiment cylinder composition	29
Table 4.4: Flux detector locations	30
Table 5.1: Specific fission rate of U-235, normalized to a trap power of 60 MW.....	37
Table 5.2: Thermal (<1.25 eV) flux [n-cm ⁻² -sec ⁻¹].....	38
Table 5.3: Fast (>1.25 eV) flux [n-cm ⁻² -sec ⁻¹]	38
Table 5.4: Fast to thermal flux ratios and the percent change.....	39
Table 5.5: Effective delayed neutron fraction and mean neutron generation time	50
Table 12.1: The ρ values and the percent error over burnup.....	73
Table 12.2: The ρ values and the percent error for varied OSCC angles and burnup..	74
Table 12.3: Error associated with the fission/s/g for each lobe.....	75
Table 12.4: Percent error for the flux values in the HEU 94CIC model.....	75
Table 12.5: Percent error for the flux values for 35/20 TRIGA [®] Model 1	76
Table 12.6: 35/20 TRIGA [®] Model 1 lobe power values and percent error.....	77
Table 12.7: HEU lobe power values and percent error	77
Table 12.8: Pin power values and percent error for 35/20 TRIGA [®] Model 1.....	78
Table 12.9: Axial power factors and percent error for 35/20 TRIGA [®] Model 1	79
Table 12.10: Radial power factors and percent error for 35/20 TRIGA [®] Model 1.....	80
Table 12.11: Eff. delayed neutron fraction and mean neutron generation time error ..	80

Reactor Physics Model of the Advanced Test Reactor using TRIGA[®] Fuel through Application of Serpent 2

1 INTRODUCTION

Beginning in 1978 with the development of the Reduced Enrichment for Research and Test Reactors Program (RERTR), the United States set out to reduce the amount of high enriched uranium (HEU) used in civilian research reactors [1]. In 2004, the U.S. Department of Energy introduced the Global Threat Reduction Initiative (GTRI) [2]. This endeavor, which incorporated and revitalized the RERTR program, was created with the intent to reduce the amount of nuclear material that could potentially be used for nuclear weapons. One of the goals under this initiative is to convert civilian research and test reactors from HEU (>20 wt-% ^{235}U) fuel to a substitute low enriched uranium (LEU) (<20 wt-% ^{235}U) fuel. A significant number of the research and test reactors that originally utilized HEU fuel have converted their cores to an LEU fuel form. However, a select number of reactors pose additional engineering design complications and therefore have yet to be converted.

Among the remaining reactors awaiting conversion are numerous facilities that currently employ fuels that contain uranium loadings much larger than that currently available in LEU form. Reactors that fall in this category are considered high performance research reactors (HPRRs). There are five United States reactors that fall under the HPRR category. One of these U.S. HPRRs is the Advanced Test Reactor (ATR) located at the Idaho National Laboratory (INL).

The ATR is a $250 \text{ MW}_{\text{th}}$ high flux test reactor powered with HEU (93.0 wt-% ^{235}U) fuel that has a maximum thermal neutron flux of approximately $1.0\text{E}+15 \text{ n}\cdot\text{cm}^{-2}\cdot\text{s}^{-1}$ with an approximate maximum fast flux of $5.0\text{E}+14 \text{ n}\cdot\text{cm}^{-2}\cdot\text{s}^{-1}$ [3]. The ATR has a unique core design that consists of 40 fuel elements, each containing 19 cylindrically curved, concentrically arranged fuel plates. The 40 fuel elements are positioned

against one another to create a serpentine core pattern, commonly referred to as a ‘four leaf clover pattern’. This pattern, or lattice configuration, results in the ability to create very high neutron fluxes where desired within the core region. The ATR’s unique geometry and design enables it to facilitate large power offset levels across the radial direction of the core [4].

1.1 Motivation

The ATR presents the GTRI and RERTR programs with unique challenges for fuel conversion due to its geometry and operating conditions. The current ATR fuel utilized to date is a UAl_x powder dispersion fuel. There are many possible fuel designs that plausibly support the ATR’s conversion from the current HEU-based fuel to an LEU fuel composition, one of which is a uranium-molybdenum ($U_{10}Mo$) monolithic fuel. The Fuels Development (FD) Program located at the INL is currently working toward the qualification of this proposed fuel composition due to its many advantageous characteristics. The FD Program has been working on the research and development of this monolithic fuel for several years [5]. The program’s efforts are very clearly identified and progress is diligently being made toward the ultimate goal of submitting a fuel qualification report to the Nuclear Regulatory Commission (NRC) for approval of use in research and test reactors. Unfortunately, the qualification of a nuclear fuel is protracted in nature and as such takes a significant amount of time, regardless of the effort being directed toward its success. In addition to the large, long-standing goal of qualifying a complex fuel such as $U_{10}Mo$ is the inherent need to develop infrastructure, technology, and the qualification of a fuel fabrication line suitable to keep up with the demand of the currently deployed fleet of research and test reactors which need this LEU fuel; the fuel fabrication necessity further delays implementation of a prototypic fuel such as the proposed $U_{10}Mo$.

An alternate, plausible substitute approach to convert the ATR in a more expeditious manner is to leverage already qualified ‘off-the-shelf’ fuels that satisfy GTRI’s goals.

Such goals include (1) the continued reactor performance characteristics currently held by each facility while, (2) meeting all reactor specific safety requirements [6].

Although unconventional, one standardized fuel composition is the uranium zirconium hydride based fuel which is most commonly utilized in TRIGA[®] reactors. Furthermore, fuel fabrication technology and infrastructure are currently deployed and in use for an application such as this. However, in contrast to the traditionally considered, plate-type fuel that the ATR currently uses, TRIGA[®] fuel is of cylindrical form posing concern from a design and safety perspective. General Atomics, the owner of the TRIGA[®] fuel concept, has demonstrated the safe use and operation of its fuel in many research and test reactors throughout the world for nearly a half of century, testifying to its inherent reliability. Therefore, if concern is drawn toward safety in an early conceptual study as this, it is most appropriately posed on the fuel's impact toward a given reactor rather than the reactor's impact on the fuel. This poses the question: if the reactor core's geometry is maintained the same, and each fuel element maintains the same external geometric envelop, or geometry, could the implementation of cylindrical TRIGA[®] fuel within a given element's envelope maintain desired reactor performance characteristics?

1.2 Objective

This study centers on design optimization of a select number of modified ATR element configurations through use of TRIGA[®] fuel within each element's overall envelope. The objective of this study is to characterize several unique fuel element configurations within the ATR core and acquire nuclear parameters at the beginning of core life (BOL) and the effective burnup of the core given a prescribed burnup rate and outage periodicity. The DOE Naval Reactors program delineates eight functional requirements for the ATR [7]; five of these requirements will be addressed here and are as follows:

- Generate a sufficient thermal flux to generate at least $4.8E+14$ fissions/s/g ²³⁵U.

- Maintain the fast to thermal flux ratio within 5% of current values within each flux trap.
- Maintain a constant power in corner lobes during a cycle.
- Achieve an operational cycle length of 56 days at 120 MW thermal.
- Keep the current core and fuel element external envelope geometry unaltered.

This study will consider six configurations of standard TRIGA[®] fuel rods arranged logically within the envelope of an ATR fuel element. Based on standard TRIGA[®] fuel, fabrication diameter of each rod is pre-established, therefore, three parameters will be varied herein:

- Rod-to-rod pitch.
- Rod-to-rod arrangement (relative position).
- Number of rods within the fuel element.

The desired core performance will be compared against a configuration of the HEU ATR core simulated by Serpent 2, which has been used in other LEU fuel feasibility studies at INL [8,9,10]. The comparison will be performed via flux levels and reactor kinetics parameters in each flux trap position. A comparison will be made against the current HEU model via steady state and depletion calculations and will include the characterization of several parameters: k_{eff} (effective multiplication factor), β_{eff} (the effective delayed neutron fraction), Λ (mean neutron generation time), thermal flux, fast flux, and power per rod in addition to the aforementioned requirements set by the Naval Reactors program. All of these parameters will be found at the beginning of core life, using the steady state solution, except k_{eff} and corner lobe power over a cycle; k_{eff} will be tabulated over the course of the core lifetime and corner lobe power will be tabulated over the course of one 56-day cycle. All predicted reactor performance characteristics are computed through use of the three-dimensional, continuous energy Monte Carlo reactor physics burnup calculation code, Serpent 2.

1.3 Document Overview

This document is organized in the following manner:

Chapter 1: Introduction – Introduction to the problem addressed by this study, motivation behind this study, and several tasks that have been addressed prior to completion of this study.

Chapter 2: Survey of Literature – Background information, survey of various reactor physics computational tools available for use as well as a survey of efforts toward the qualification of the proposed $U_{10}Mo$ fuel as compared against TRIGA[®] fuel.

Chapter 3: Advanced Test Reactor Overview – High level overview of the ATR along with technical and functional core design aspects which impact and relate to a reactor physics study.

Chapter 4: Models and Methodology – Detailed description of the HEU model and the six proposed potential configurations studied, analyzed, and discussed herein as well as a description of the methodology for which this analysis was performed.

Chapter 5: Results and Discussion – Comparison of the models developed in this study against the HEU model and presentation of reactor performance parameters for each model. The results are accompanied by a discussion of observations made with respect to each model.

Chapter 6: Conclusions – Concluding remarks concerning this study.

Appendices, references, and a list of variables are provided at the end of this document for the reader's convenience.

2 SURVEY OF LITERATURE

Many factors impact and influence the nuclear characterization of a reactor including the computational tools utilized during a study along with the methodology and rigor leveraged while performing the analysis. This chapter discusses a select number of available computational tools, which are often used for reactor performance characterization including strengths and weaknesses of each. In addition, a discussion of the current efforts directed toward the qualification of the proposed $U_{10}Mo$ monolithic fuel and a qualitative comparison between the proposed fuel's strengths and weaknesses relative to the currently qualified TRIGA[®] fuel will be made with context being directed toward implementation within the ATR.

2.1 Computational Reactor Physics Tools

There are several reactor physics codes available that may be harnessed to characterize desired reactor core parameters while also performing depletion calculations. A few of these computational tools include the Monte Carlo N-Particle code (MCNP), the Oak Ridge Isotope Generation and Depletion code (ORIGEN), the Standardized Computer Analyses for Licensing Evaluation (SCALE), Attila, HELIOS, KENO, CASMO, SIMULATE, and Serpent [11,12,13,14,15,16]. These reactor physics and transport computational tools may be broken down into two general categories (1) deterministic neutronics modeling (e.g. CASMO/SIMULATE, HELIOS, SCALE, Attila) and (2) stochastic neutronics modeling (e.g. MCNP, KENO, Serpent) [17]. There are advantages and disadvantages to both methods. Deterministic models iterate explicitly or solve implicitly the equations of interest and provide a discrete solution that is reproducible from one study to the next. Because stochastic codes are statistical in nature, a given solution may not be repeated explicitly from study to study, but rather a solution within statistical error may. Regardless, stochastic codes are much more commonly utilized within the nuclear community and as such yield direct access to and use of evaluated nuclear data [16].

2.1.1 Deterministic Computational Tools

Deterministic codes such as CASMO/SIMULATE, HELIOS, SCALE, and Attila solve the equations of interest directly. They require that the evaluated nuclear data files (ENDF) be processed into multigroup data via lattice codes (CASMO, HELIOS, and SCALE) for the solution of discretized equations. Once the group cross section information has been generated, the data may then be applied using reactor physics codes (SIMULATE and Attila) [18,19]. Reactor physics codes are usually based on nodal diffusion methods, which divide the reactor geometry into homogenized regions, or nodes, and then by characterizing node-to-node leakage a full-scale core simulation may be obtained [19,20]. Attila employs an iterative method to solve the neutron transport equation via linear discontinuous finite-element spatial differencing [18] which results in a rigorously defined solution at every point within the domain. Early in the development and progression of the nuclear industry the deterministic approach was the most practical method for which computational reactor physics studies were performed; the relatively recent increase in computing capabilities that enabled stochastic computational tools to solve these problems within reasonable time frames has made these tools more prevalent [19].

2.1.2 Stochastic Computational Tools

Stochastic codes often leverage the Monte Carlo technique in order to develop neutron histories using evaluated nuclear data files until a statistically significant solution is obtained. This method is a simple way to very accurately characterize a system.

Serpent is a continuous-energy stochastic transport code; it differs slightly from the aforementioned stochastic codes primarily due to the methods it utilizes when performing neutron tracking functions. Traditionally, neutron tracking is done by tracking each neutron until it reaches either a new collision site or a material boundary, then it recalculates the distance to the next boundary, and the process is repeated. This process can result in lengthy computation times. Serpent uses the Woodcock delta tracking method [21]. This method uses a global majorant cross

section* [21], which is equal to the largest total cross section in the system in order to calculate the probability of a collision. The material total cross section over this global majorant cross section gives the probability of collision in that material; if that collision is rejected by that probability it results in a ‘virtual’ collision and a new path length is calculated and the neutron path continues [21]. This neutron tracking method eliminates the need to recalculate new surface boundary distances when a neutron reaches a material boundary, which results in faster calculation times. This is a distinct advantage in cases of complex geometry.

There are downsides to this method however; the common way to calculate reaction rate integrals in Monte Carlo codes such as MCNP, by using the track length estimator, can no longer be used because the neutron paths now extend over material boundaries and the discontinuous points (the virtual collisions) are unknown. The alternative to this method is a collision flux estimator which, rather than summing the neutron track lengths, sums over all collisions in a specified area. This method results in poor efficiency for small regions of optically thin material, regions of low collision density, and systems with void regions.

Another disadvantage to the delta tracking method is that in regions where there are large differences between the material total cross sections, the collision sampling process becomes inefficient since the probability of sampling a real collision within the low material cross section regions is low. The inefficiency issues introduced by the delta tracking method are compensated for in the actual implementation of the geometry routine by also utilizing the traditional neutron tracking technique when the inefficiencies of the delta tracking method become too high (i.e. when collision sampling efficiency is low) [21].

* Global majorant cross section is defined as $\Sigma_{\text{maj}}(E) = \max\{\Sigma_{\text{tot},1}(E), \Sigma_{\text{tot},2}(E), \dots, \Sigma_{\text{tot},M}(E)\}$.

2.1.3 Depletion Methodology

At the time in which the study had begun, the most recent version of MCNP was that of MCNP version 5 (MCNP5). MCNP5 requires the use of a supporting fuel burnup computational tool such as ORIGEN [12,13]. In addition to MCNP5 an alternate code which performs depletion calculations is SCALE. SCALE also requires the use of add-ons to perform depletion computations; one code that supports the depletion computation when interacting with SCALE is the TRITON (Transport Rigor Implemented with Time-dependent Operation for Neutronic depletion) code sequence, T-DEPL [11]. Serpent has built-in burnup calculation routines that compare favorably to more widely used codes like CASMO while maintaining reasonable calculation times [15].

The burnup calculation in Serpent is made up of two steps: the transport cycle and solving the Bateman equations, which describes the concentration of specific isotopes over time and is shown in equation 2.1,

$$\frac{dN_j}{dt} = \sum_{i \neq j} \lambda_{ij} N_i - \lambda_j N_j, \quad N_j(0) = N_0 \quad j = 1, \dots, n \quad 2.1$$

where j represents a given nuclide, n is the total number of nuclides, N_j is the atomic density of nuclide j , and λ_{ij} are the transmutation coefficients which characterize decay and neutron-induced reactions. The transport cycle step determines the rate of transmutation via neutrons using Monte Carlo techniques. The rate of transmutation reactions and nuclear library data (i.e. decay constants and fission product yields) can then be used to solve the Bateman equations. Transmutation coefficients used in these equations are corrected (since these are assumed constant over a burn step) by using the “predictor-corrector” method which averages together predicted material compositions and those that result from the transport calculation. The predictor-corrector method thus allows for larger burn steps [15,22]. This process uses updated material compositions from the solved Bateman equations and repeats. In order to solve the resulting set of Bateman equations, Serpent uses a matrix exponential solution.

Serpent's burnup calculations have been compared with those of CASMO-4E, which has a depletion model similar to that of Serpent but has a different routine for equilibrium xenon calculation [15]. This comparison shows that for burn step sizes ≥ 2.5 MWd/kgU the ^{135}Xe concentrations begin to differ and starts to be reflected in the k_{∞} values at burn steps near 15 MWd/kgU. Discrepancies in the k_{∞} values between the two models are also caused by a difference in the ^{149}Sm saturation value. Overall, while the CASMO-4E and Serpent have comparable results for k_{∞} and material compositions they also have noticeable differences in build-up rates for fission product poisons.

Serpent's burnup calculation was also compared to MonteBurns, a coupling code for MCNP5 and ORIGEN2. The burnup routine for MonteBurns differs from that of Serpent via its predictor-corrector method. Rather than averaging the predicted material compositions with final material compositions, MonteBurns stops the solution midway through the current step and uses this to recalculate the material compositions [23]. The study that compared these two codes accounted for this by running each code without the corrector step, but the study ultimately had inconclusive results as far as consistency of calculated values. The analysis did prove useful in comparing calculation times; while MonteBurns took 40 hours to complete the calculation, Serpent took 67 minutes [15].

2.1.4 Computational Tools Closing

Serpent has a number of advantages over the competition. Along with having built-in depletion capabilities, Serpent uses a number of features to speed up calculation time such as utilizing Woodcock delta-tracking to simulate neutron histories [16] as well as the ability to perform parallel computation. Additionally, it features an advanced plotting feature that enables not only the plotting of reactor geometry but also thermal flux and fission rate. Serpent also has additional geometries available such as the "pad" surface type that is defined by an angle of a cylinder between two radii to form a three dimensional arc [24]; the diversity in the available surface geometries decreases the complexity of the input deck.

2.2 Core Fuel Development and Qualification

2.2.1 Research Reactors

As previously mentioned, the FD Program was created within the RERTR Program to support the U.S. HPPRs in their conversion from HEU to LEU fuel. As a part of the FD Program's work scope, a fuel development and qualification plan was created to facilitate and guide the qualification of a uranium-molybdenum fuel. The RERTR fuel development and qualification plan consisted of first conducting preliminary scoping studies, irradiating small coupon sized irradiation samples (a.k.a. miniplates) and evolving the study to eventually full sized plate irradiations with the intent to generate fuel performance data. While these tests occurred, fabrication processes and techniques were concurrently developed. Presently, it is proposed that large scale testing of entire fuel elements representative of fuel geometry and operating conditions of specific reactors will be inserted as irradiation experiments to facilitate full-sized proof of concept and provide a demonstration of the proposed fuel's integration into an integral element form [5,25].

In addition to the this generic fuel qualification effort, neutronic feasibility studies have been performed for each of the U.S. HPRRs to provide a feasibility analysis on whether a conversion to LEU would be plausible and if so, what alterations to current core configurations need to take place to maintain acceptable core performance characteristics. An example of this includes the feasibility study for the High Flux Beam Reactor (HFBR) using a diffusion theory code called DIF3D, which was validated via MCNP. The results of this particular study found that the HFBR was not viable for LEU conversion but the HFBR has since been decommissioned for unrelated reasons [26]. In addition to the HFBR, neutronic feasibility studies conducted on the six remaining unconverted HPRRs, including the High Flux Isotope Reactor (HFIR), National Bureau of Standards Reactor (NBSR), the University of Missouri Columbia Research Reactor (MURR), the ATR, the ATR critical facility (ATRC), and the Massachusetts Institute of Technology Reactor (MITR) [27,28,29,12,30], show promising results for conversion feasibility; none however

have been converted to LEU fuel. A presentation given by Stevens [31] reviews the challenges that face the high performance research reactors in converting to LEU; these high-density designs must withstand high heat flux, high burnup, and high coolant flows. Current research is focused on extensive neutronics and thermal hydraulics modeling in order to mitigate the issues with converting the remaining research and test reactors to LEU.

2.2.2 The Advanced Test Reactor Conversion

Extensive studies have gone into potential fuel designs for the ATR LEU conversion. Multiple feasibility studies and evaluations of different core modeling techniques have gone into finding suitable replacement fuel [14,12]. The studies thus far have focused on a U-Mo monolithic fuel type with various neutron control mechanisms such as having integral clad burnable absorbers, hafnium shimming within the clad, or cadmium wires within element side plates [14,32]. The company responsible for INL and the ATR, Battelle Energy Alliance (BEA) has offered the support necessary to upgrade the current fuel fabrication process for LEU U-Mo research reactor fuel [33].

3 ADVANCED TEST REACTOR OVERVIEW

The ATR core comprises forty, wedge-shaped fuel elements arranged in a serpentine pattern, illustrated in Figure 3.1, creating nine flux trap regions of localized peak neutron flux levels. In these regions, flux values presently reach upwards of $1\text{E}+15$ $\text{n}/\text{cm}^2\text{s}$ at thermal energy level(s) and $5\text{E}+14$ $\text{n}/\text{cm}^2\text{s}$ at fast energy level(s). Each element, illustrated in Figure 3.2, contains nineteen fuel plates. These plates are a highly enriched uranium dispersion fuel type, clad in aluminum, and are poisoned with boron incorporated within the fuel matrix to control excess reactivity. The fuel meat has a nominal width of 0.508 mm with a nominal clad thickness of 0.381 mm. Each element is 1682.75 mm in length with an active fuel length of 1219.2 mm. Each element has coolant channels between each plate that are between 1.295 mm and 1.956 mm wide [34].

The ATR operates at a nominal pressure of 2.5 MPa (360 psig) and fluid temperature of 71°C (160°F) with a maximum, licensed operating power of $250 \text{ MW}_{\text{th}}$. Presently, the ATR operates most commonly at a steady power of approximately $120 \text{ MW}_{\text{th}}$. The ATR is capable of maintaining a nominally constant axial power profile through the use of hafnium outer shim control cylinders (OSCC), which do not offset power axially, only radially. Power allocation radially across the core is manipulated through a combination of rotating these drums and inserting shim rods, which can create a power ‘tilt’, or power offset, across the core of up to 3:1 [8]. This offset provides the capability of running simultaneous experiments under different test conditions. The ATR has a total of 77 different experimental irradiation positions; each position is 1.2 m long and ranges from 1.3 to 13 cm in diameter. In the conversion from HEU to LEU it is paramount to maintain these parameters within an acceptable window in order to preserve the unparalleled experiment capabilities of the ATR.

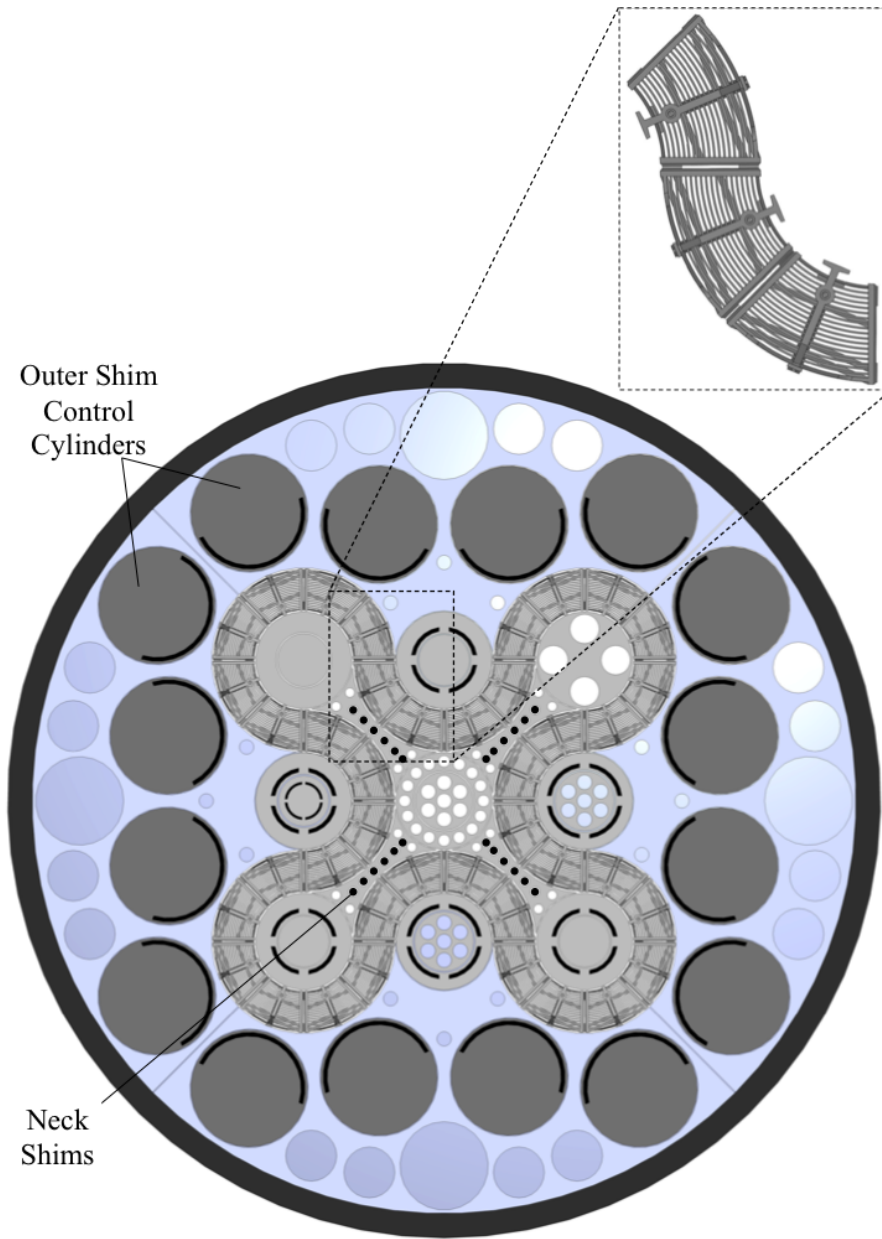


Figure 3.1: Advanced Test Reactor core cross section

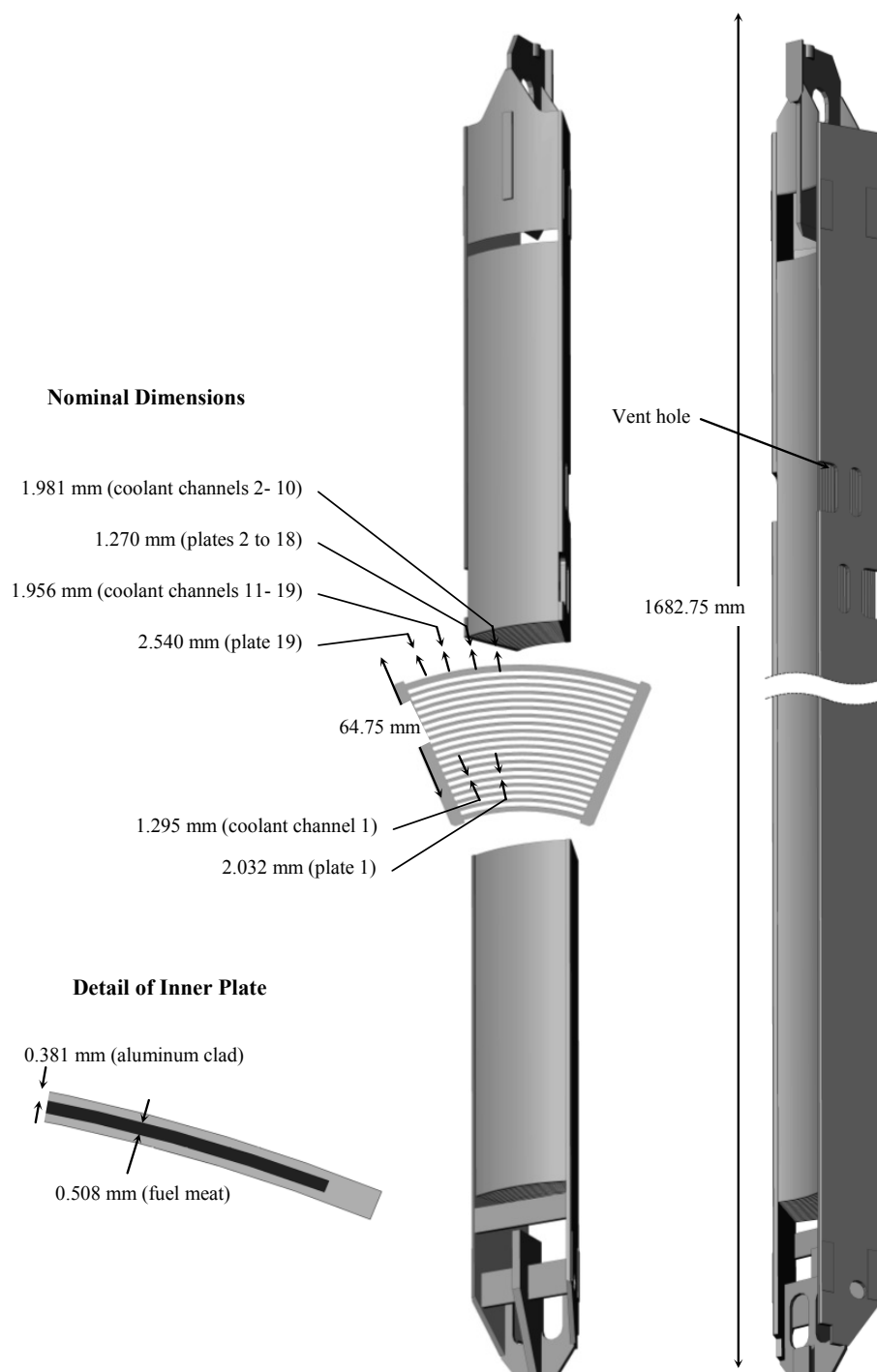


Figure 3.2: Pictorial view of ATR fuel element

4 MODELS AND METHODOLOGY

Six unique geometric configurations of the ATR were developed in an effort to analyze the effects of rod number and rod placement; all models considered contain TRIGA[®] fuel rods. Each model was compared against a baseline model, the current ATR HEU core. The comparison includes k_{eff} over a simplified core lifetime, thermal flux, and thermal to fast flux ratios. Additionally, integral element power is presented for thermal hydraulic context. All flux and eigenvalue results are from collision estimates. For all models, the ENDF/B-VII library was used for all nuclear data at 300K.

4.1 Baseline Model

The HEU model of the ATR, which has been used as the benchmark to compare the TRIGA[®] fuel models against, was developed at the INL and is based on the 1994 core internals change-out core configuration (94CIC). The baseline model, graphically shown in Figure 4.1, has demonstrated good agreement with measurement data within the range of propagated nuclear data uncertainties [35] and is therefore considered to be a credible representation of the current ATR operating state, including reactor performance characteristics.

As seen in Figure 4.1, all experimental irradiation facilities were included in the geometric representation, each of the 16 OSCCs were positioned with the same rotation angle relative to the core, and all elemental geometric characteristics were included into the core region.

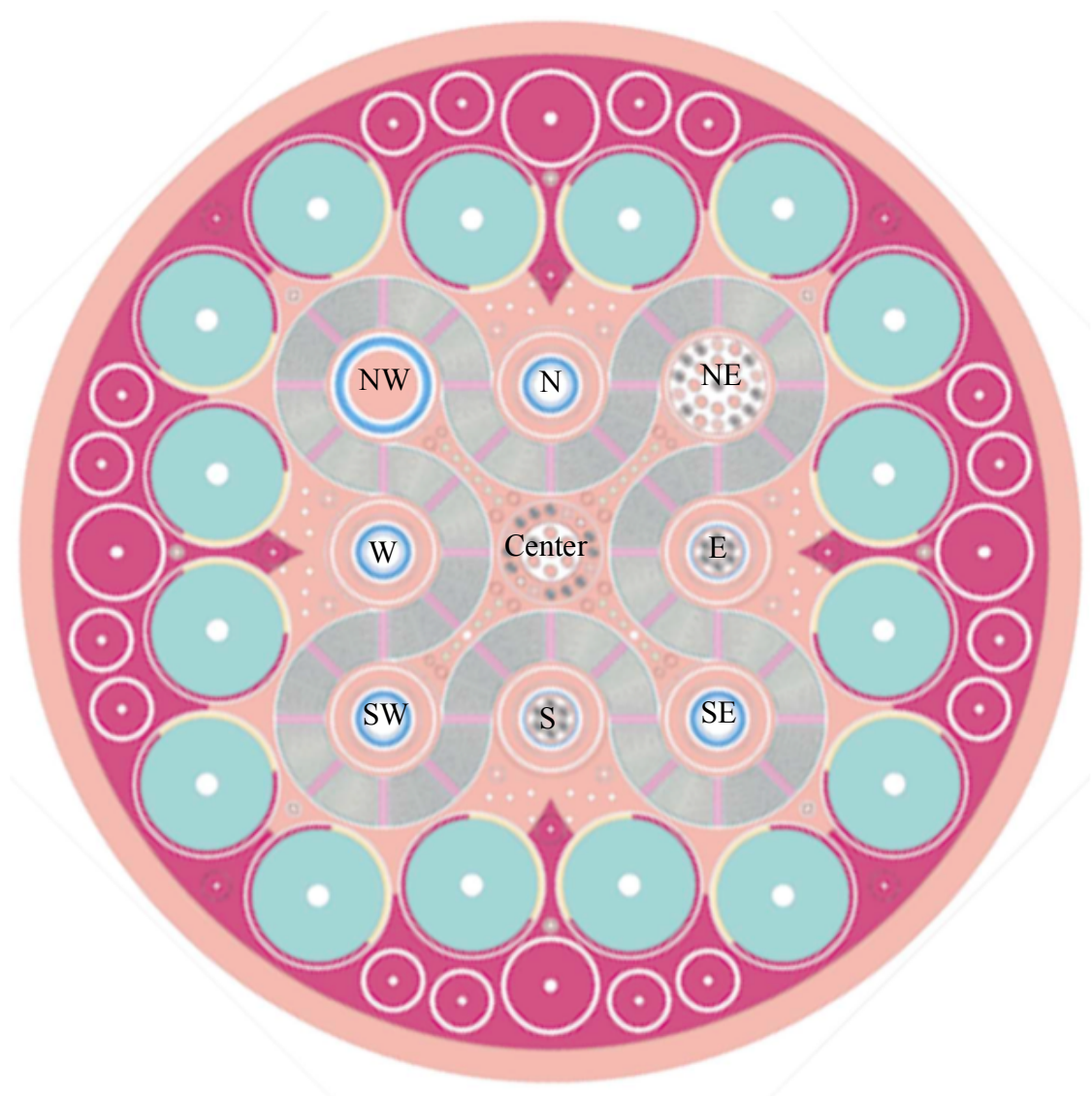


Figure 4.1: HEU ATR model

4.2 TRIGA[®] Fuel

General Atomics (GA) has presented the possibility of manufacturing their uranium-zirconium hydride (UZrH) TRIGA[®] fuel rods for implementation within high performance reactors through a feasibility study of the MIT research reactor [36]. A U.S. NRC nuclear regulation (NUREG-1282) [37] depicts all acceptable ranges of material composition for which GA's UZrH fuel may be applied within research and tests reactors in the U.S. These ranges are noted in Table 4.1.

Table 4.1: Variables for TRIGA[®] fuel rod composition [36,37]

Characteristic	Value
Uranium content (mass %)	8.5-45
Uranium-235 enrichment (mass % U)	<20
Ratio of H to Zr	1.58-1.65
Cladding material	SS-304
	Incoloy 800H
	Aluminum 1100F

The fuel rods used in the models developed as a part of this study have a fuel meat radius of 0.573 cm, a length of 121.92 cm, and a cladding thickness of 0.04 cm. Note that this radius is much smaller than the standard TRIGA[®] fuel rod radius of 1.8 cm and the advantage to using a smaller radius is in reducing the effect of self-shielding within the fuel rods. Fuel of this geometric form (reduced radius) has been fabricated and already implemented within the existing 14 MW_{th} Romanian TRIGA[®] Reactor.

TRIGA[®] fuel is often loaded with 1.1 wt-% erbium, which provides the support for pulsing capabilities; this additional absorber is not necessary for inclusion within the design of a non-pulsing reactor and as such has been omitted from consideration as a part of this study [38].

The fuel compositions used in the models analyzed here were down selected from the continuous spectrum of available choices shown in Table 4.1 and are tabulated in Table 4.2. TRIGA[®] fuel is most commonly clad in stainless steel (SS); in the relatively lower power TRIGA[®] reactors, aluminum cladding has been employed; however with the longevity of UZrH fuel within a low power research reactor, corrosion, and blistering has been shown as a credible risk when utilizing aluminum cladding. The advantage of having a more robust clad material such as stainless steel in the case of higher power research and test reactors outweighs the complications that come from activated stainless steel during fuel shuffling and reloading as compared to aluminum clad. An alternate cladding option for TRIGA[®] fuel is that of Incoloy-800H which has

been implemented within the fuel configuration of the Romanian reactor exclusively. This potentially viable option was also considered as a part of this study's considerations when investigating potential fuel compositions as seen in in Table 4.2.

In order to identify an appropriate hydrogen-to-zirconium ratio to be utilized through the majority of this study, a sensitivity analysis was conducted on its impact to maintain a critical state within the core during a simplified standard cycle. The study was performed using 30/20 fuel with stainless steel clad. This study's outcome is presented in Appendix A. In the sensitivity study, three hydrogen-to-zirconium ratios were chosen (the most extreme upper and lower bounds that the fuel is licensed for, along with the mean of the two). The results demonstrated no significant impact on the reactor's ability to maintain a steady critical state, however, it did in fact alter the potential core life by approximately 400 MWdays which ultimately may extend and provide significant benefit to the ATR through further optimization. Regardless, for this study a ratio of 1.6 was chosen as this is a common ratio employed within most TRIGA[®] reactors presently [39].

During conduct of this study, each configuration (from Table 4.2) was considered; however, results from the configuration containing 35/20 fuel are presented in the primary body of this document as it demonstrated the most potential for implementation within the ATR. All other configurations demonstrated an inability to meet one or more of Naval Reactor's functional requirements established as a part of this study's objectives; these results are presented within Appendix B. Included within these limiting characteristics:

- The 30/20 fuel composition yielded an insufficient cycle length
- The 45/20 fuel with the Incoloy 800H cladding was not further analyzed here due to issues detailed in Appendix B.
- The 40/20 and the 45/20 fuel compositions with the stainless steel cladding resulted in supercritical cores with no shutdown margin.

Table 4.2: TRIGA fuel rod compositions

Characteristic	30/20	35/20	40/20	45/20	45/20
Uranium content [Mass %]	30	35	40	45	45
Uranium-235 enrichment [Mass % U-235]	19.7	19.7	19.7	19.7	19.7
Ratio of H to Zr	1.6	1.6	1.6	1.6	1.6
Cladding material	SS-304	SS-304	SS-304	SS-304	Incoloy 800H

4.3 TRIGA[®] Fuel Models

4.3.1 Model 1

To investigate the feasibility of TRIGA[®] fuel within the ATR, the most compact arrangement of pins was modeled and was the starting part for all subsequent models and is shown in Figure 4.2. Model 1 is composed of 21 fuel rods. Four concentric ringlets make up a single element configuration with four elements located in the innermost ring, five in the second, and six in the third and outermost rings. As all of models presented herein were developed via a blind calculation method, the intent was to develop a single model (Model 1) that comprises the most fissile material that may functionally be placed within an ATR element's envelope. The following models were developed by reducing the number of rods within the element and configuring the rods strategically to acquire specific insight regarding their relative location within an ATR element envelope.

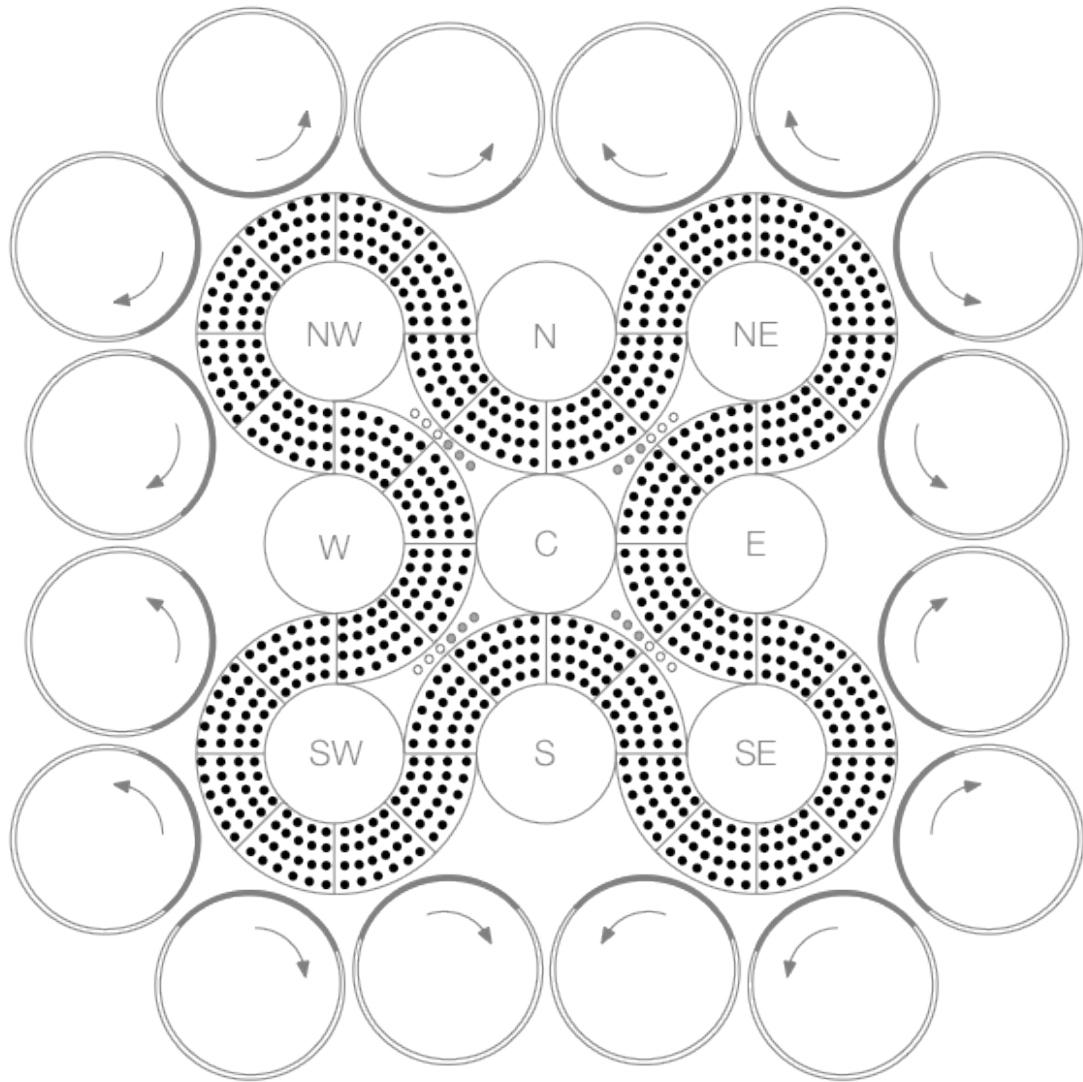


Figure 4.2: Sketch of a top-down view of Model 1

4.3.2 Model 2

Model 2, shown in Figure 4.3, consists of 15 fuel rods, where the outermost (longest) ring of rods has been eliminated from Model 1 in order to both reduce the number of rods within each element envelope but maintain rods in close proximity to the flux traps. The asymmetric nature of this configuration may cause non-negligible flow disparities across the core from a thermal hydraulic perspective, however, pushing the

fissile material toward each flux trap will provide much larger flux values in the central region (toward the inside of each element) as compared to the exterior region (toward the OSCCs).

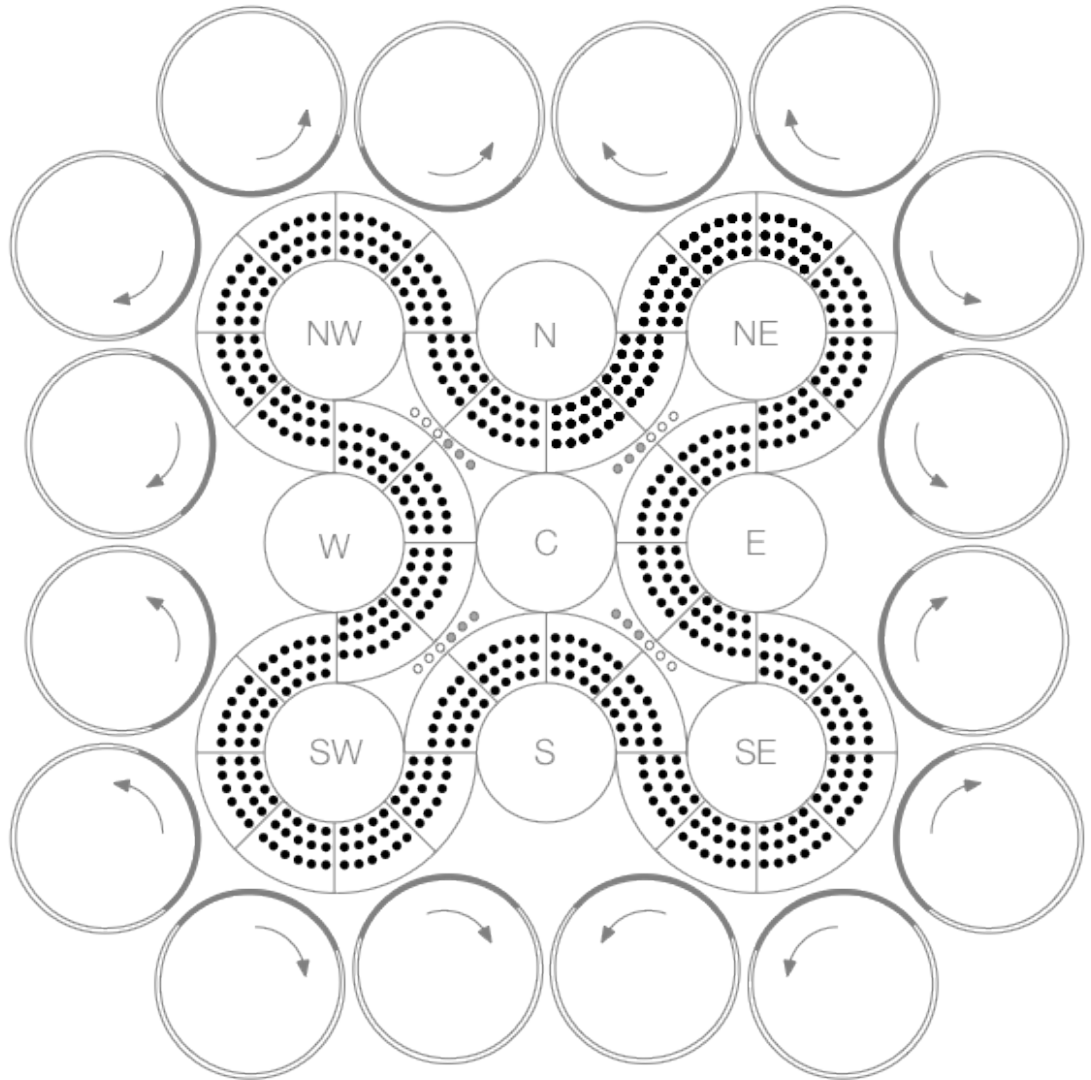


Figure 4.3: Top-down view of Model 2

4.3.3 Model 3

Model 3 attempts to replicate Model 2, however, it reduces the potential for flow disparity by pushing the rods slightly away from the flux traps to create a centrally arranged elemental configuration.

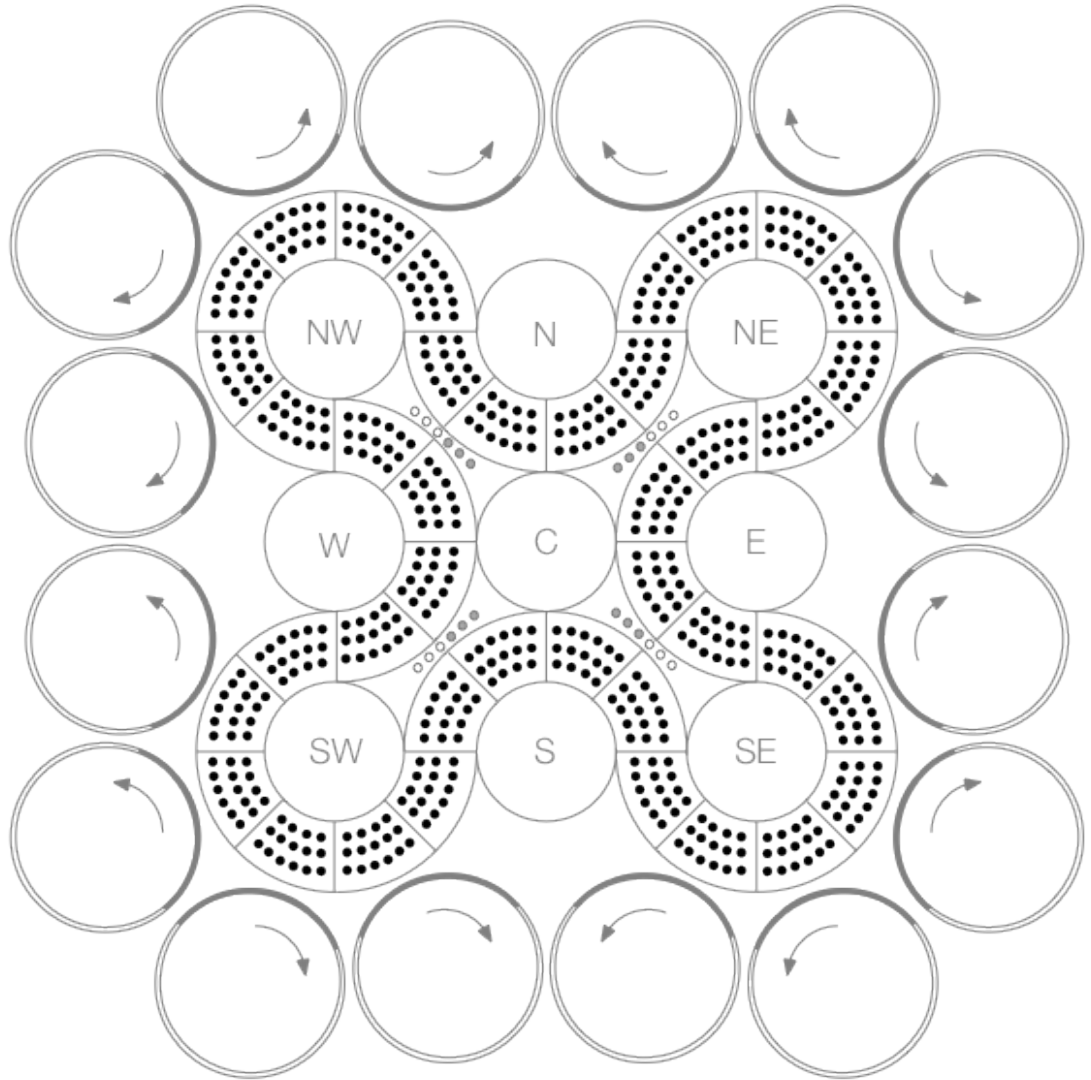


Figure 4.4: Top-down view of Model 3

4.3.4 Model 4

Model 4, shown in Figure 4.5, is an attempt to replicate Model 2 in its fuel rod proximity to the flux traps, but retain core symmetry. To do this arrangement, elements surrounding the center flux trap contain 17 fuel rods while the remaining elements contain 15 fuel rods. Additionally, this model differs from Model 2 in that the center flux trap will see an increase in local neutron flux levels in the center core region due to the relative proximity of additional fissile material.

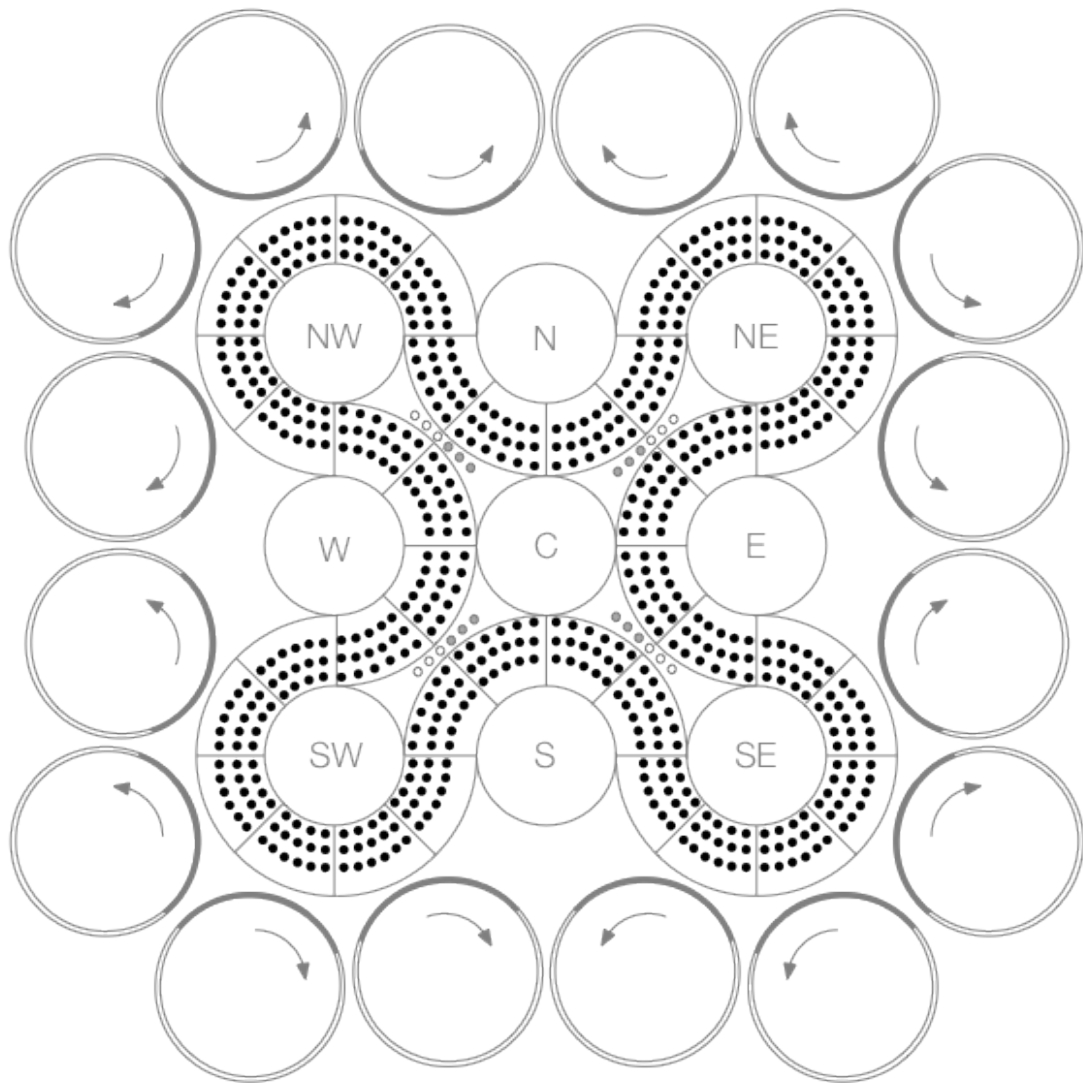


Figure 4.5: Top-down view of Model 4

4.3.5 Model 5

Model 5, shown in Figure 4.6, contains 14 fuel rods per element envelope and provides further analysis of sufficient criticality with regards to the reduction of rods. This model, when compared against the alternate models demonstrates the potentially large thermal flux values in the interior regions of the envelopes as a result of neutron thermalization from the additional moderator material.

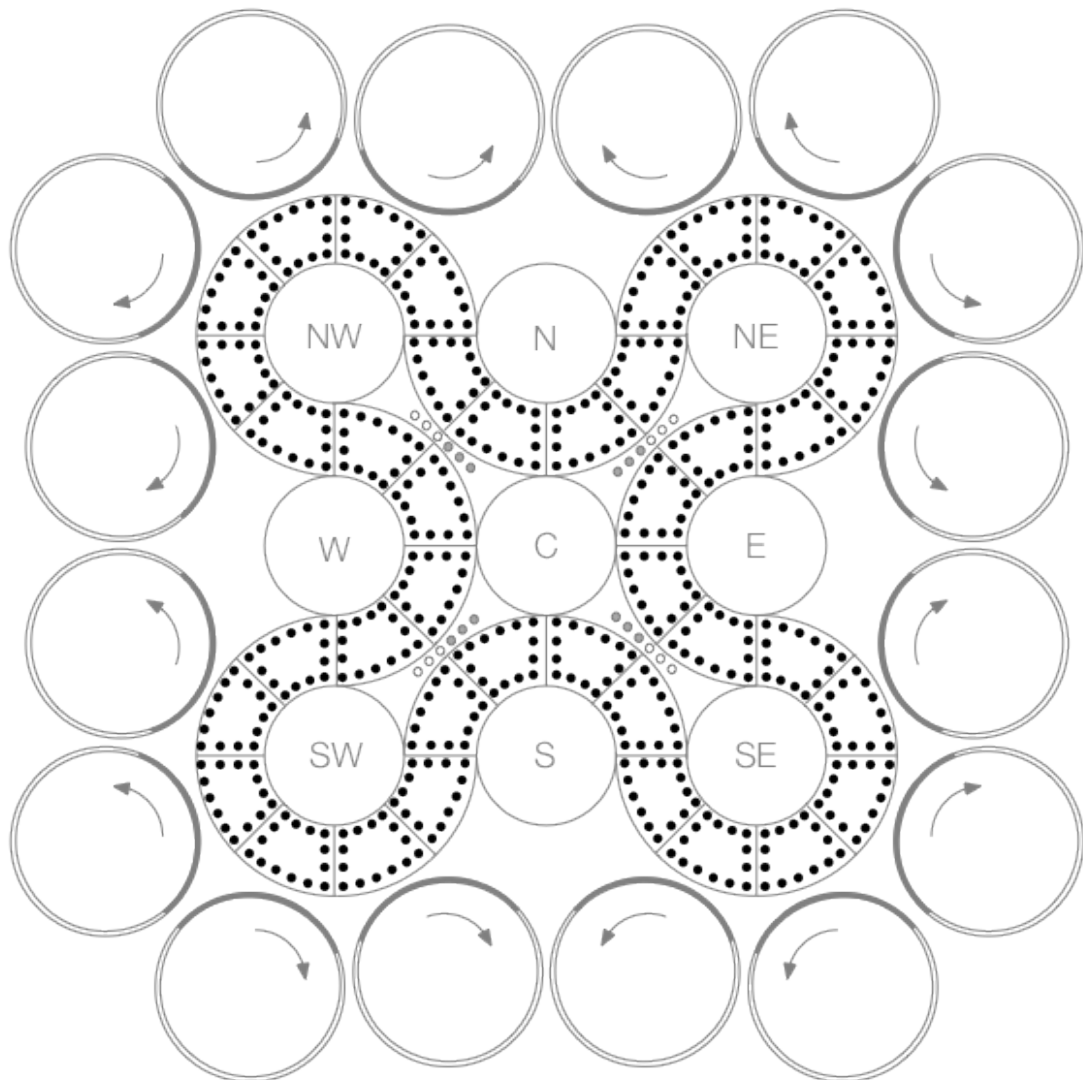


Figure 4.6: Top-down view of Model 5

4.3.6 Model 6

Model 6, shown in Figure 4.7, contains 17 fuel rods per element envelope and provides an intermediate comparison between Model 2 and Model 4 with respect to number of rods and rod placement.

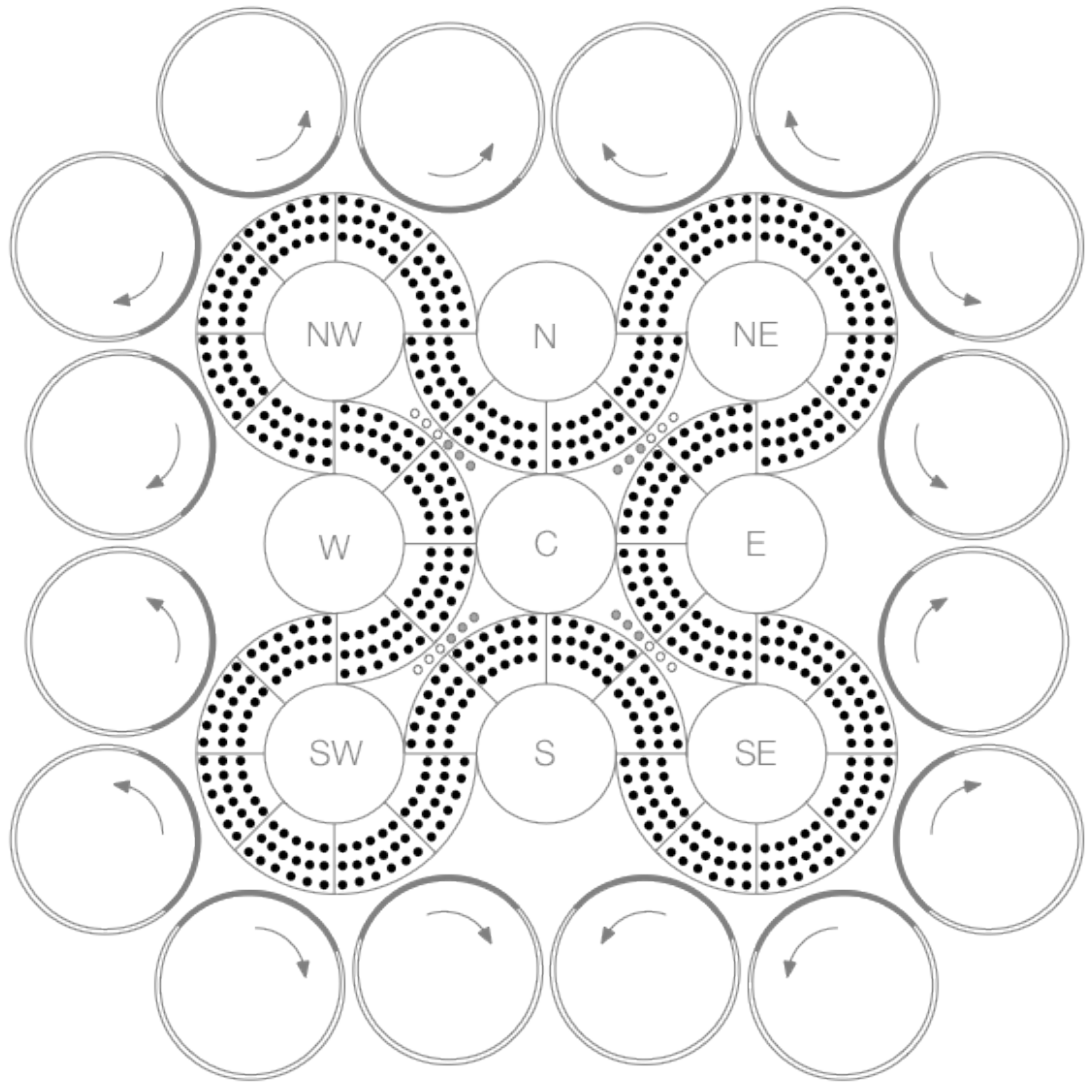


Figure 4.7: Top-down view of Model 6

4.4 Reactor Characterization

In order to simplify the characterization of these models, a sensitivity analysis of the OSCC rotation was performed in order to remove models that were not viable due to a lack of or excess in reactivity for the 30/20, 40/20 and 45/20 fuel compositions, which can be found in Appendix B. Once reactivity of the core was established given discrete rotation angles for all OCSSs at BOL, depletion calculations were performed in order to verify feasibility of the remaining models with regards to cycle length. For the 35/20 fuel composition, the OSCC analysis was performed after the depletion analysis in order to incorporate the OSCC worth dependence on burnup. Viable models were then characterized via the specific fission rate of ^{235}U , thermal flux, fast flux, fast to thermal flux ratio, flux trap and trap neutron spectrum, corner lobe power over a 56-day cycle, power per rod, axial and radial rod power profiles, effective delayed neutron fraction (β_{eff}), and mean neutron generation time (Λ).

4.4.1 Depletion Analysis

Initially, all six TRIGA[®] models, using the 45/20 fuel with stainless steel cladding, and the HEU 94CIC model had their burnup calculations performed at an arbitrary OSCC rotation of 60° with zero out of 24 shim rods inserted in order to establish a general burn-up rate for each model. This data, found in Appendix B, shows that Model 1 is the only model to have sufficient fissile material to last the entire 56-day cycle. This analysis was used to justify the analysis of only Model 1 for the 35/20 loading. Additionally, a sensitivity analysis was performed in order to assess the need for multiple burn regions within the fuel pin and can be found in Appendix C. For the HEU model and the 35/20 TRIGA[®] model, these calculations were performed using 10000 neutron histories per generation with 500 active generations and 200 skipped generations.

4.4.2 OSCC Analysis

The amount of positive reactivity inserted by the OSCCs rotating away from the core was found to be dependent on both the loading and burnup of the core. Due to this

dependence, the reactivity as a function of rotation angle was found for each burnup step. This was done in order to determine what OSCC rotation angle would be required at each burnup step in order to obtain $\rho \approx 0$, where ρ is defined in equation 4.1 and indicates how removed a core is from a critical state.

$$\rho \equiv \frac{(k_{eff}-1)}{k_{eff}} \quad 4.1$$

For the 45/20 and 30/20 models, using the burnup rates from the depletion analysis, an appropriate rotation angle for the OSCCs could be selected that would result in $\rho \approx 0$. The OSCC analysis for these models did not include the burnup dependency of the reactivity, and as a result, overestimate the positive reactivity available from the OSCCs.

The metric used to determine whether a model has sufficient reactivity across a 56-day cycle was the rotation angle of the OSCCs necessary to obtain a critical core ($\rho = 0$) at each burn interval. If a model can be made critical at all times during a 56-day cycle through the addition of positive reactivity from OSCC rotation, then that model meets the 56-day at 120 MW cycle functional requirement. If a model remained subcritical at any point in a 56-day cycle for an OSCC rotation angle of 180° , that model did not meet the 56-day, 120 MW minimum functional requirement.

4.4.3 Specific Fission Rate of ^{235}U

In order to determine if the model has a sufficient thermal flux, the specific fission rate [fissions/s/g] of ^{235}U is calculated. To find this value, a 60.96 cm (24 in) long, 0.28615 cm radius cylinder was placed in the SE and SW in-pile tube (IPT) experiment position, shown in the center of Figure 4.8.

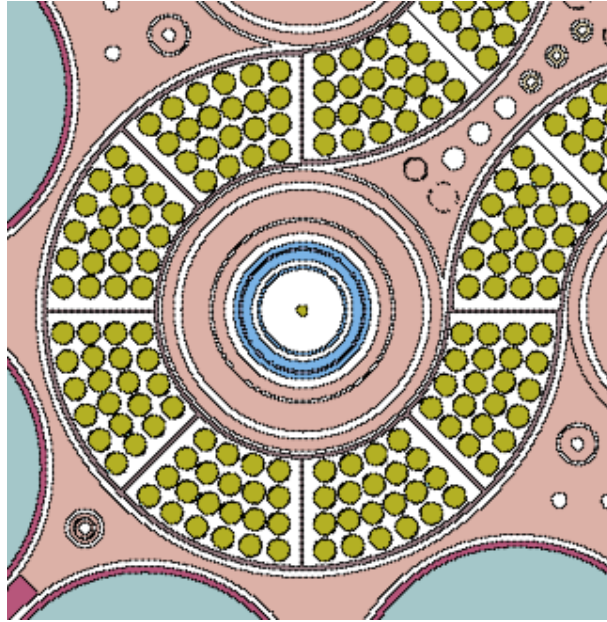


Figure 4.8: The SW IPT with the experiment cylinder

The cylinder's composition matched that of the HEU model plate five's composition and is tabulated in Table 4.3. This composition and cylinder geometry were designed such that there is 1 gram of ^{235}U per linear inch of the cylinder, which simplifies the translation between number of fissions and specific fission rate.

Table 4.3: Specific fission rate experiment cylinder composition

Nuclide	Atomic Density [atoms-b ⁻¹ -cm ⁻¹]
^{234}U	4.23430E-5
^{235}U	3.92110E-3
^{236}U	1.46940E-5
^{238}U	2.35210E-4
^{27}Al	5.12370E-2

To obtain an adequate thermal flux to produce the minimum requirement of $4.8\text{E}+14$ fissions/s/g ^{235}U in the HEU core set forth by Naval Reactors, a lobe power of 60 MW is typically required [7]. Because there are four independent lobes that may have a power tilt, operating all four quadrant lobes at 60 MW would yield an integral power

of 240 MW. However, this study operates on a 120 MW steady state power level assumption. To find this value without implementing a 3:1 power tilt across the model, the specific fission rate is found in the SE and SW traps without the power tilt; the value is then normalized to 60 MW. This normalization is done by first summing the power of the eight elements associated with each lobe to obtain lobe power, then dividing specific fission rate by the lobe power. Multiplying by 60 MW renormalizes the specific fission rate value for a new lobe power of 60 MW.

4.4.4 Neutron Flux Analysis

The neutron flux values were obtained in the nine different core locations, and tallied within these material regions. The specific locations are provided in Table 4.4 (and are graphically depicted in Figure 4.1). These locations were chosen as they are central locations within each flux trap and represent a variety of target configurations. A briefly paraphrased description of each target configuration may also be found in Table 4.4.

Table 4.4: Flux detector locations

Flux Trap Location	Description
Northwest (NW)	Central aluminum
North (N)	Central water
West (W)	
Southwest (SW)	
Southeast (SE)	
Northeast (NE)	Water around targets in central zone
Center (C)	
East (E)	Water around targets
South (S)	

The neutron flux was tallied in both the SCALE 238-group structure to obtain a spectrum and a 2-group structure with a division at 1.25 eV to compare fast and thermal flux values.

4.4.5 Corner Lobe Power

In order to prevent unwanted power ramping and temperature transients in fueled specimens within experiment positions, the corner lobe powers are required to remain nominally constant over the duration of a cycle. To ensure that the lobe powers were constant over the course of a cycle, the power for each lobe was obtained by summing their associated element powers at 7-day intervals for one 56-day cycle.

4.4.6 Further Model Characterization

The power per rod was obtained for the first five fuel elements of each viable model. This was determined to be of sufficient resolution due to the 1/8 core symmetry of the ATR and the symmetry of the models. The fission energy deposition, used as a means to obtain power during a steady state calculation, was tallied in 20 axial regions and 10 radial regions of the highest power rod.

The effective delayed neutron fraction and the mean neutron generation time across a 56-day, 120 MWd cycle were also tabulated as a means of further characterizing the model. These values were obtained directly from the Serpent output file.

5 RESULTS AND DISCUSSION

Results presented within this chapter are specific to the HEU 94CIC model, as well as Model 1 containing 35/20 fuel with stainless cladding.

5.1 Depletion Analysis

A depletion calculation was performed on Model 1 and the HEU model at an arbitrary OSCC rotation (60°) in order to establish the general burnup trend, shown in Figure 5.1, using 10000 histories per generation for 500 active generations and 200 skipped generations. Once the burnup rate for the first 56 days of the core lifetime was established, the BOL k_{eff} was used in order to determine objectively an OSCC rotation that resulted in an average k_{eff} in slight excess of unity over the first 120 MW cycle.

The preliminary results obtained from the 45/20 and 30/20 models show that in order to obtain a critical core at BOL, 20 (of the available 24) neck shims must be inserted into the 35/20 model. Based on a 35/20 fuel composition, with four neck shims removed, the reactor shutdown margin at BOL was found to be approximately \$1.50; presently the requirement is \$5.80 [40]. A neck shim rod was withdrawn from each quadrant at each subsequent burn step (7 days) until all of the neck shims had been removed; this occurred at 35 operational days. This was done in an attempt to compensate for burnup of fissile material and burn-in of poisons in order to maintain a relatively flat criticality state versus burnup, allowing for the small remaining compensation of reactivity to be provided by the OSCCs.

The rotation angles for the OSCCs of 60° were used to obtain the data presented in Figure 5.1, where the HEU model has 3 neck shims per quadrant inserted over the entire 56-day cycle.

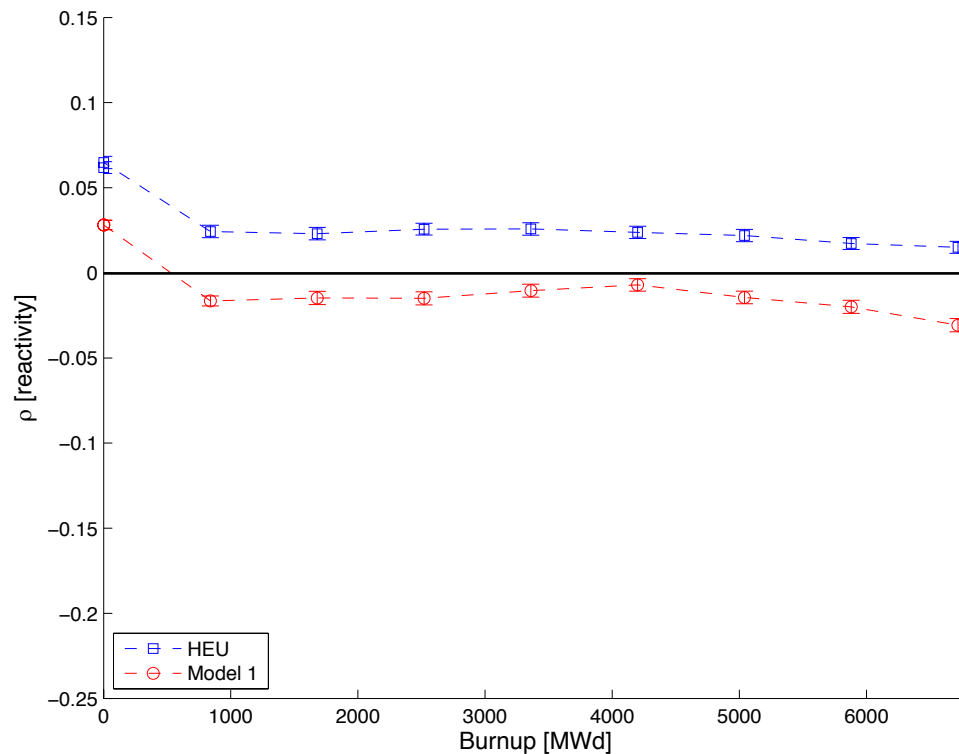


Figure 5.1: Depletion calculation of the HEU 94CIC and TRIGA[®] Model 1

The buildup of ^{149}Sm to its equilibrium concentration is partially the cause of the nonlinear portion after the initial ^{135}Xe drop in the HEU model. Model 1 stays fairly steady, if not increasing slightly, until day 35 when the last neck shim is removed and Model 1 begins a burnup trend slightly steeper than that of the HEU model. The percent error associated with results presented in Figure 5.1 may be found in Appendix D, section 12.1.

5.2 OSCC Analysis

The OSCC analysis for Model 1 at each burnup step of the 56-day, 120 MW cycle was performed using 10000 histories for the 0 MWd analysis and 1000 histories for all subsequent burn steps, each with 500 active generations and 200 skipped generations. For the 0 MWd OSCC analysis, the reactivity as a function of rotation angle was obtained directly from Serpent calculations for each rotation angle. The reactivity as a

function of rotation angle for subsequent burn steps was generated by obtaining the reactivity at a single rotation angle using the burned material compositions from the depletion analysis in the previous section. Using the difference between the reactivity of the 0 MWd burn step and the reactivity at a single rotation angle in the subsequent burn steps (0° OSCC rotation angle except for the 6720 MWd burn step which uses the 180° OSCC rotation angle), the reactivity for other rotations could be inferred. The resulting OSCC analysis is shown in Figure 5.2. The percent error associated with the results presented in Figure 5.2 may be found in Appendix D, section 12.2. Additionally, it should be noted that each one of these burn steps had neck shim rod configurations consistent with that presented in Figure 5.1 for Model 1.

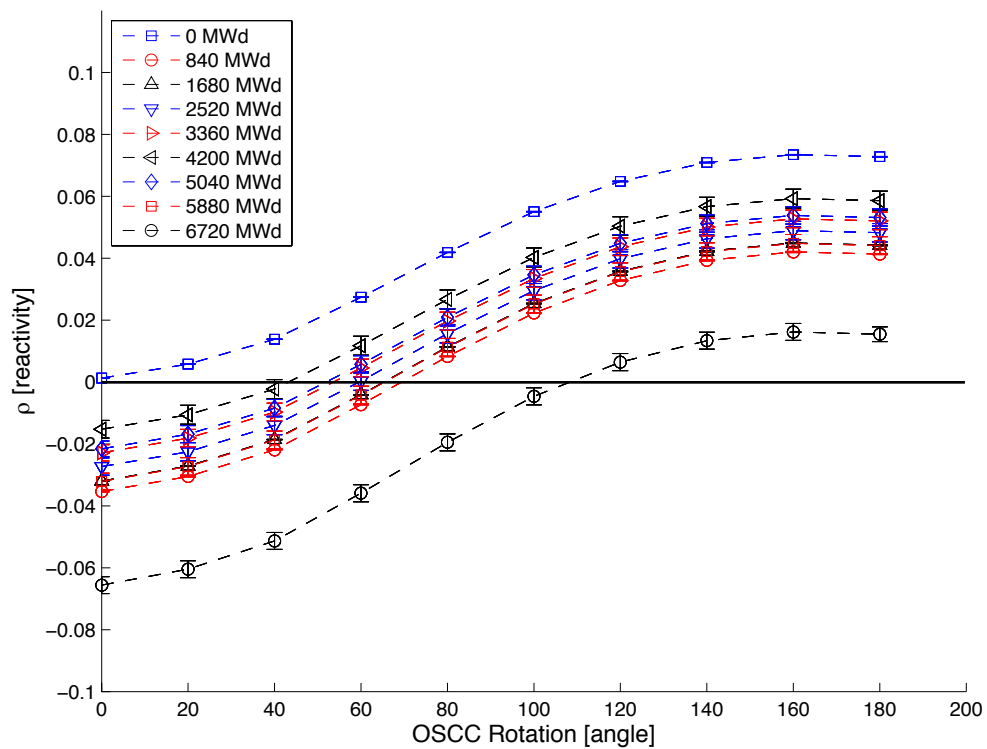


Figure 5.2: Reactivity vs. OSCC Rotation for 35/20 TRIGA fuel

The 180° OSCC rotation angle for the EOC reactivity calculation was used in order to ensure (based on Serpent output, not data extrapolation) that Model 1 of the 35/20

TRIGA[®] fuel has enough reactivity to last the entire 56 day, 120 MW cycle. Since the 180° OSCC rotation angle proved to provide enough positive reactivity to make Model 1 supercritical, this indicates that Model 1, using 35/20 fuel, has sufficient reactivity to last a 56-day cycle. The k_{eff} value at the end of the 56-day cycle, for an OSCC rotation angle of 180°, and with no neck shims inserted is 1.01570 ± 0.00243 .

Using the extrapolated reactivity values from Figure 5.2, the OSCC rotation angle necessary to provide $\rho \approx 0$ was plotted for each burnup step and is shown in Figure 5.3.

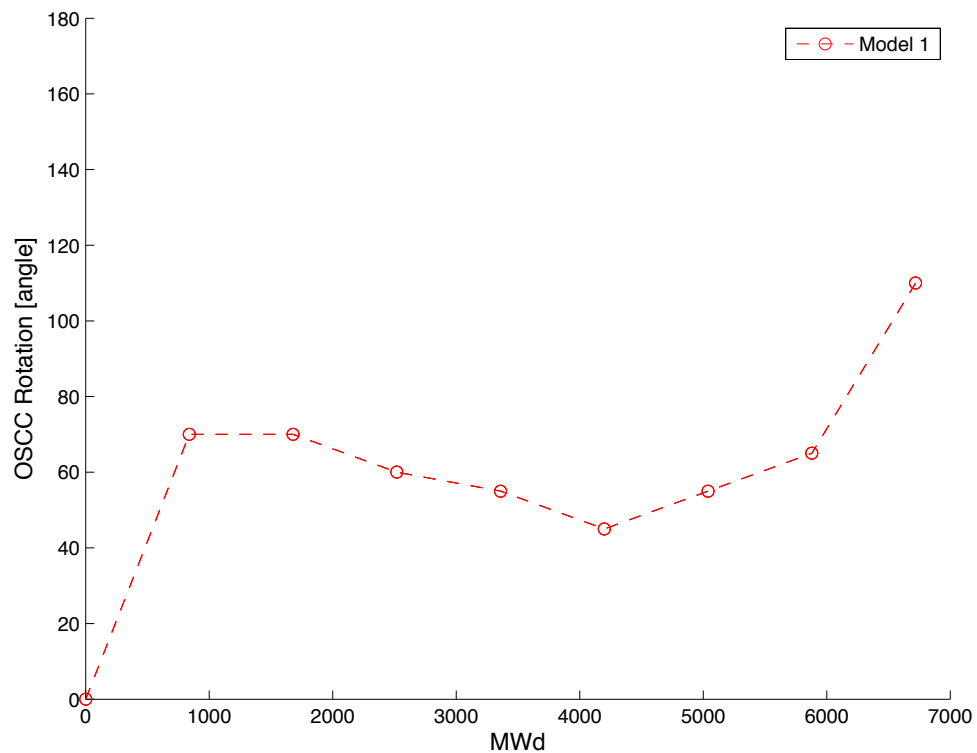


Figure 5.3: OSCC Rotation vs. MWd for 35/20 TRIGA fuel

The large initial rotation angle is likely a combination of compensation for ^{135}Xe burn in at BOL and a need to rotate the OSCC more near the smaller OSCC angles in order to compensate for the angles nearer 0° and 180° having a smaller differential worth. After the initial increase, there is a slight downward trend in the required OSCC

rotation angle due to the slight upward trend in k_{eff} that results from neck shim withdrawal. After all the neck shims are removed at 4200 MWd, k_{eff} begins to drop and positivity reactivity is required from the OSCCs so the rotation angle increases accordingly. The smaller differential worth combined with OSCCs that are worth less at EOC make for a large final OSCC rotation.

Model 1 using 30/20 fuel was found to last only up to 35 operational days with no neck shims inserted and an OSCC rotation angle of 180° and Model 1 using 45/20 fuel proved to be supercritical even at BOL, all neck shims inserted and an OSCC rotation angle of 180° (see Appendix B).

5.3 Specific Fission Rate of ^{235}U

A parameter of interest is the specific fission rate. Table 5.1 presents the tabulated values for the specific fission rate of ^{235}U for a lobe power of 60 MW. These calculations were performed with 10000 histories per generation for 1000 active generations for the HEU model and 5000 histories for 500 active generations for Model 1. The percent error associated with these values may be found in Appendix D, section 12.3. Recall that one of the requirements that Naval Reactors set forth as a part of the conversion effort was minimum specific fission rate of 4.8E14 fissions/s/g. Through inspection of Table 5.1, both the southeast and southwest traps produce acceptable values in Model 1 while the HEU core has sufficiently large specific fission rates. This reduction in specific fission rate is hypothesized to be a result of change in moderator to fuel ratio. As the present fuel design caters to a moderator to fuel ratio of approximately unity, yielding very high efficiencies, the Model 1 geometry results in a moderator to fuel ratio of greater than unity, dropping the geometric efficiency within the core region and ultimately hardening the spectrum.

Table 5.1: Specific fission rate of U-235, normalized to a trap power of 60 MW

Trap	HEU [fissions/s/g]	Model 1 [fissions/s/g]	Change [%]
SE	5.44E+14	5.01E+14	-7.91
SW	5.55E+14	4.83E+14	-13.06

5.4 Neutron Flux Analysis

In addition to specific fission rate, a requirement set forth by Naval Reactors is the thermal flux, fast flux, and the fast to thermal flux ratio. The HEU and TRIGA Model 1 thermal flux levels are shown in Table 5.2 for each discrete flux trap. The flux traps referenced in Table 5.2 are graphically depicted in Figure 4.1. From Table 5.2, it is shown that all flux traps have a drop in flux when considering the Model 1 configuration to the present configuration and fuel. This is attributed to the relative distance that the fuel material is located as compared to the flux trap position. In the present play-type fuel, Plate 1 of the 19 plate fuel element is positioned approximately 2.54 mm away from the exterior wall of the flux traps, while in Model 1, the closest fuel material is approximately 5 times the distance which therefore leads to five times the additional mean free paths through highly scattering moderator material. Similar observations may be seen in Table 5.3 given a drop in fast flux levels throughout when comparing the Model 1 configuration to the present HEU core. Another contributing factor to the lower flux levels of Model 1 is the increased effect of the resonance absorption region of ^{238}U due to the higher percent of ^{238}U within LEU. Table 5.4 presents the fast to thermal flux ratio values in each of the flux traps for the HEU (5000 histories per generation / 500 active generations) and Model 1 (60000 histories per generation / 500 active generations) configurations. A reduction in fast to thermal neutron flux ratios is observed, and in all cases but one the flux traps for the LEU Model 1 fall inside of the acceptable margin of change (less than 5 percent change). The drop is attributed to an increase in moderator to fuel ratio within each element which further enhances the thermalization of neutrons and effectively reduces the relative percentage of fast neutrons available to reach the flux trap positions.

Table 5.2: Thermal (<1.25 eV) flux [$\text{n}\cdot\text{cm}^{-2}\cdot\text{sec}^{-1}$]

Flux Trap	HEU	Model 1	Change [%]
NW	1.28E+18	1.14E+18	-11.3
SW	6.95E+17	6.13E+17	-11.9
NE	2.04E+18	1.86E+18	-9.01
SE	6.60E+17	6.09E+17	-7.73
C	1.55E+18	1.32E+18	-14.6
W	8.17E+17	7.06E+17	-13.6
E	1.93E+17	1.71E+17	-11.6
N	7.57E+17	6.42E+17	-15.2
S	1.75E+17	1.60E+17	-8.9

Table 5.3: Fast (>1.25 eV) flux [$\text{n}\cdot\text{cm}^{-2}\cdot\text{sec}^{-1}$]

Flux Trap	HEU	Model 1	Change [%]
NW	3.94E+18	3.32E+18	-15.7
SW	7.60E+17	6.66E+17	-12.4
NE	2.10E+18	1.84E+18	-12.3
SE	7.31E+17	6.52E+17	-10.7
C	1.85E+18	1.51E+18	-18.1
W	8.38E+17	6.96E+17	-16.9
E	3.48E+17	2.98E+17	-14.6
N	7.73E+17	6.40E+17	-17.3
S	3.21E+17	2.78E+17	-13.4

Table 5.4: Fast to thermal flux ratios and the percent change

Flux Trap	HEU	Model 1	Change [%]
NW	3.07E+00	2.91E+00	-5.01
SW	1.09E+00	1.09E+00	-0.60
NE	1.03E+00	9.93E-01	-3.67
SE	1.11E+00	1.07E+00	-3.24
C	1.19E+00	1.14E+00	-4.19
W	1.03E+00	9.86E-01	-3.85
E	1.80E+00	1.74E+00	-3.31
N	1.02E+00	9.96E-01	-2.50
S	1.83E+00	1.74E+00	-4.89

Figure 5.4 through Figure 5.12 provide a comparison of neutron flux spectra for the HEU core and LEU Model 1 in each flux trap position identified in Table 4.4. Through qualitative inspection of these spectra, the general trending values maintain relative consistency between both core configurations. Both the HEU and 35/20 TRIGA[®] models display a large peak dominated by the Maxwellian distribution (thermal energy region), followed by a drop through the resonance energy region and lastly an increase driven by the Watt fission spectrum (fast energy region). It is noteworthy that the HEU model spectrum compares well against other studies' results previously performed outside of this work-scope [35].

Through closer inspection, the NW trap shows the presence of a much harder spectrum than any other, which can be explained by that region's lack of moderating material. The SW trap and SE trap have nearly identical spectral characteristics; this is due to the two regions having congruent mechanical configurations in addition to their symmetry across the core. The north and the west flux traps also have congruent spectra resulting from similar conditions as described for the SW and SE traps. The error analysis and resulting error values for the neutron flux values obtained may be found in Appendix D, section 12.4.

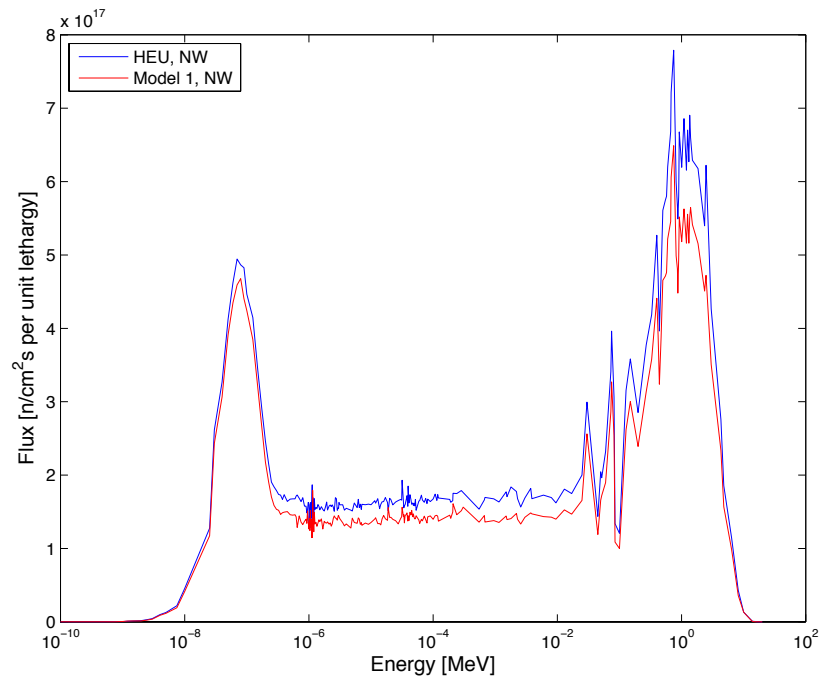


Figure 5.4: NW trap flux spectrum (per unit lethargy)

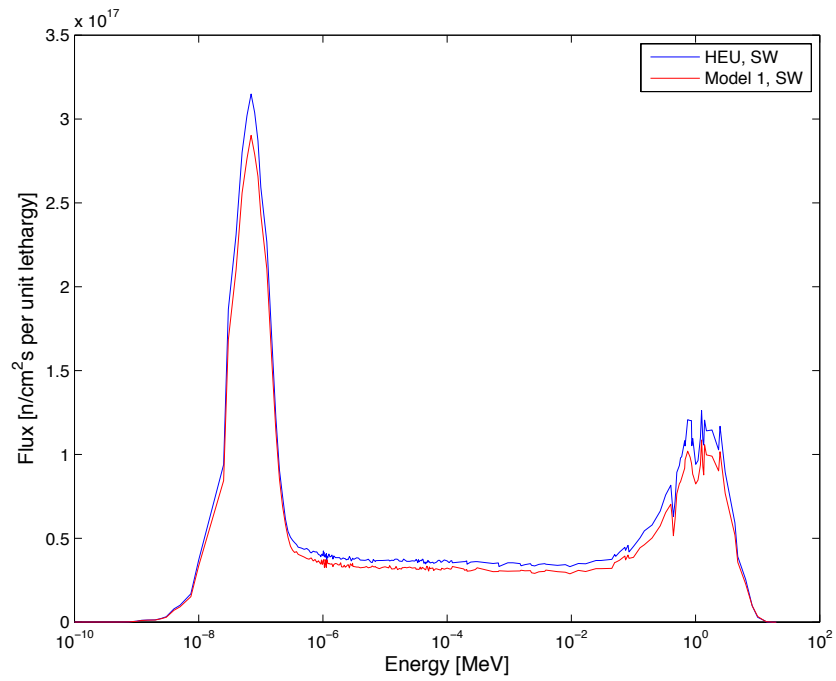


Figure 5.5: SW trap flux spectrum (per unit lethargy)

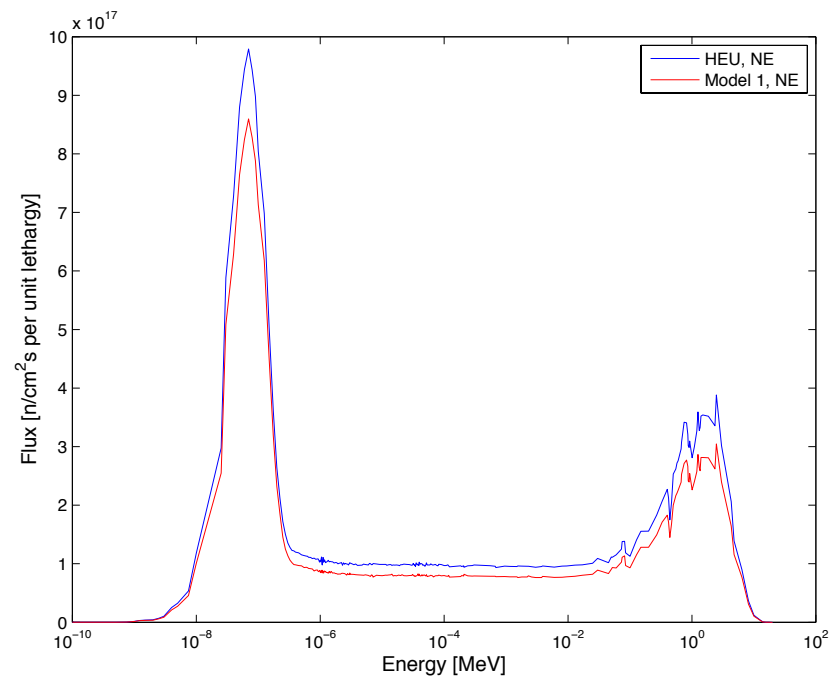


Figure 5.6: NE trap flux spectrum (per unit lethargy)

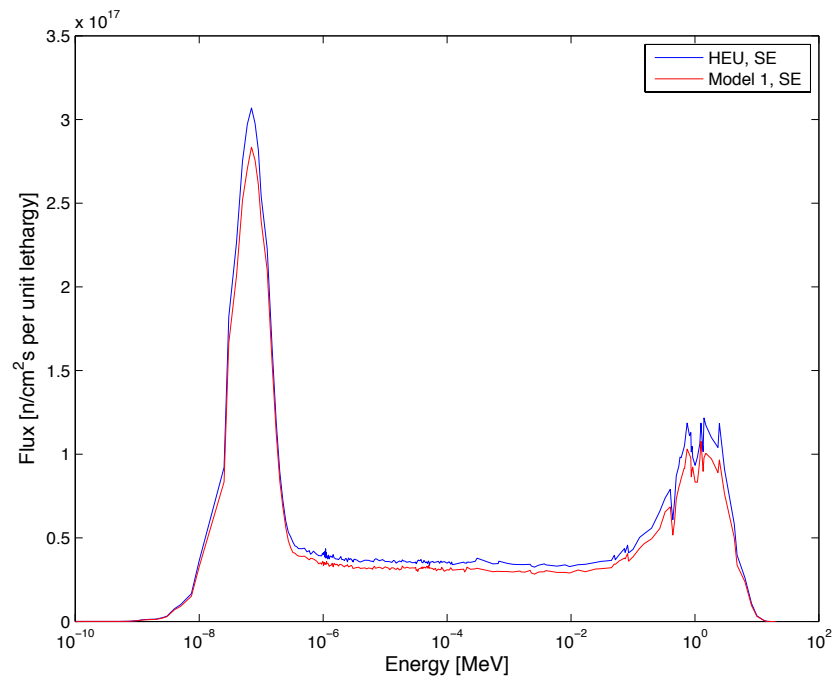


Figure 5.7: SE trap flux spectrum (per unit lethargy)

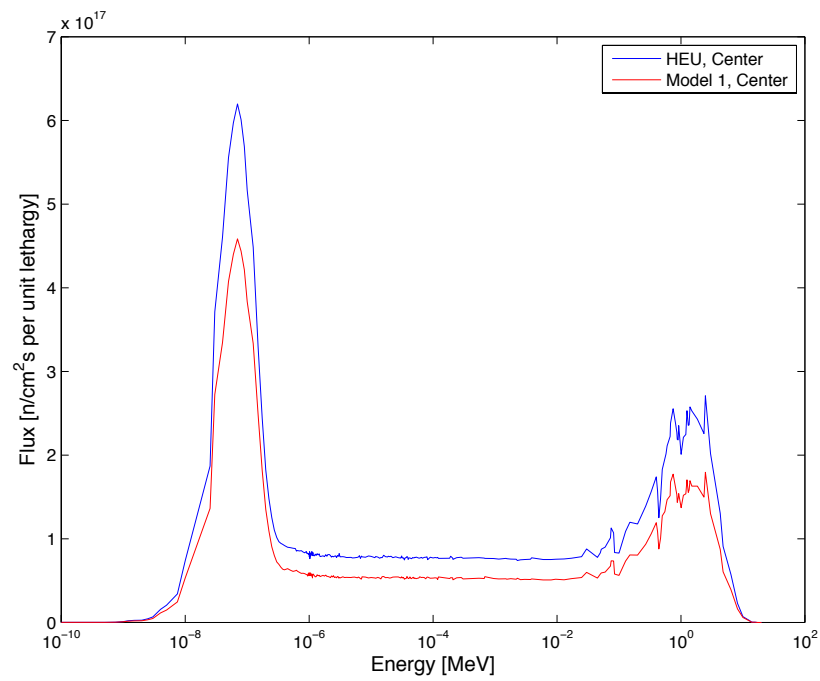


Figure 5.8: Center flux spectrum (per unit lethargy)

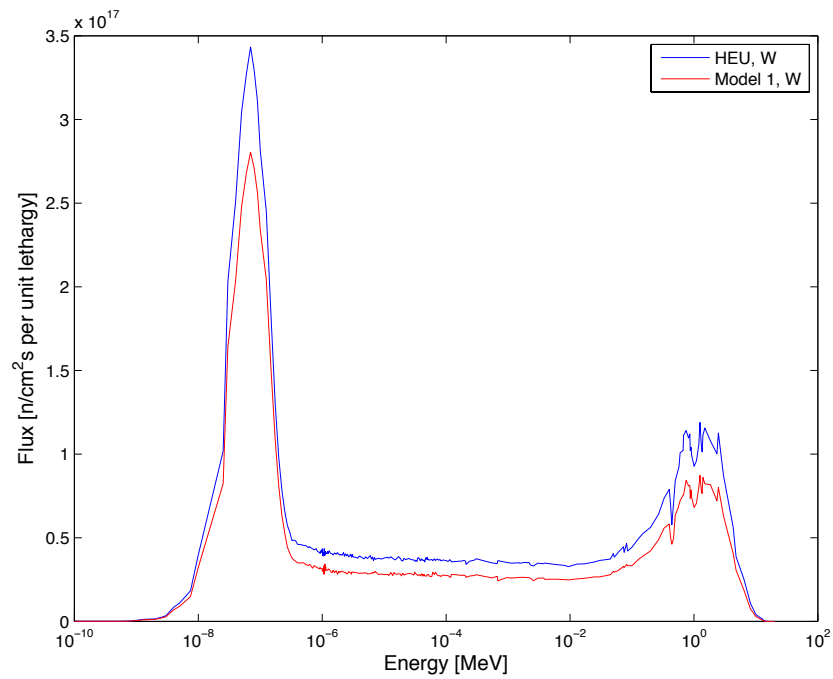


Figure 5.9: West flux trap flux spectrum (per unit lethargy)

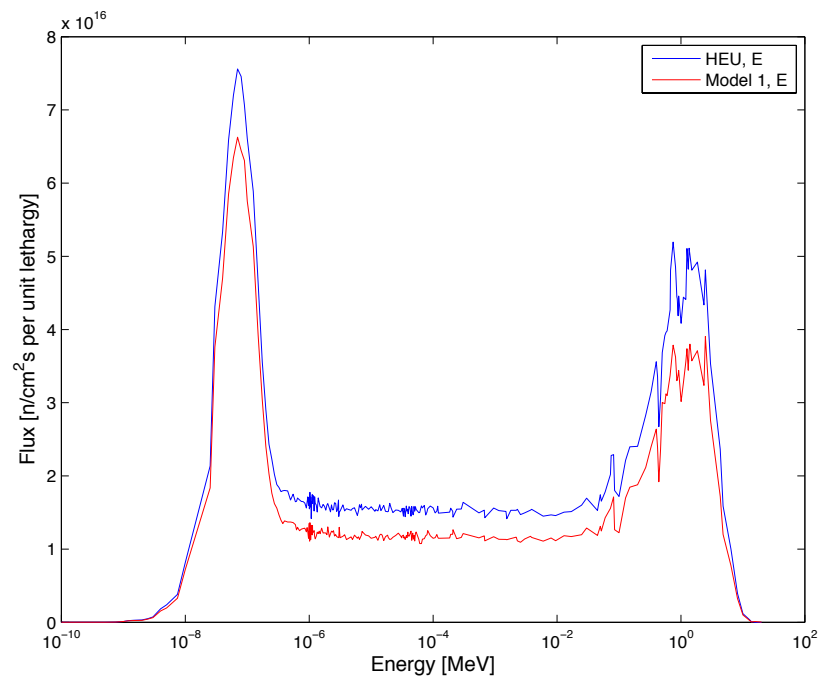


Figure 5.10: East flux trap flux spectrum (per unit lethargy)

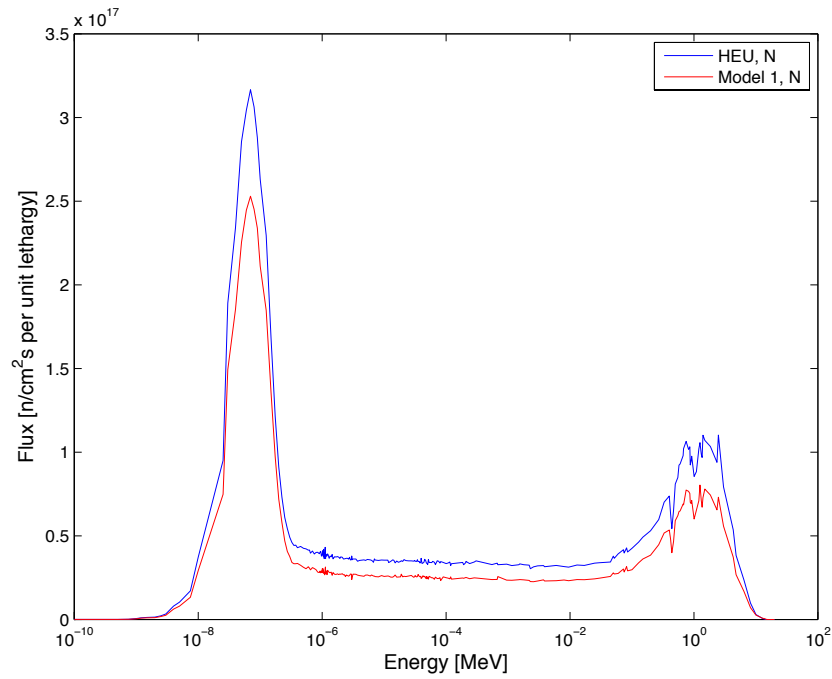


Figure 5.11: North flux trap flux spectrum (per unit lethargy)

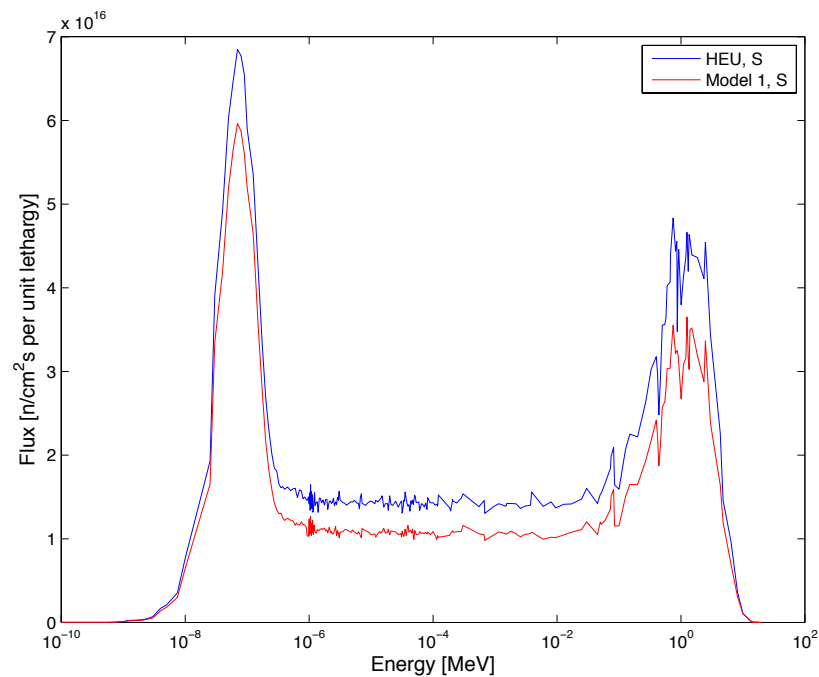


Figure 5.12: South flux trap flux spectrum (per unit lethargy)

5.5 Corner Lobe Power

The Naval Reactors functional requirements stipulate that ATR is required to maintain a constant corner lobe power across a cycle in order to prevent temperature transients within fueled specimens. Figure 5.13 plots the power in each lobe over the course of a 56-day cycle. The largest percent difference, for consecutive burn steps, in the power of the NW lobe is 3.32%, for the SE lobe the largest percent difference is 2.12%, for the SW lobe the largest percent difference is 2.83%, and for the NE lobe the largest percent difference is 2.20%. The overall decreasing trend in lobe power for all lobes is postulated to be due to a combination of shimming out the shim rods over the cycle, and an increased burn-up rate in the lobe regions near the beginning of the cycle. Both of these factors would inherently push a larger number of neutrons to fission near the center of the core at a relatively elevated level to that at beginning of cycle. The largest percent difference across the first cycle for the HEU fuel is 5.12%, in the SE

lobe. The values for the HEU power over the first cycle and the error analysis for both models can be found in Appendix D, section 12.5.

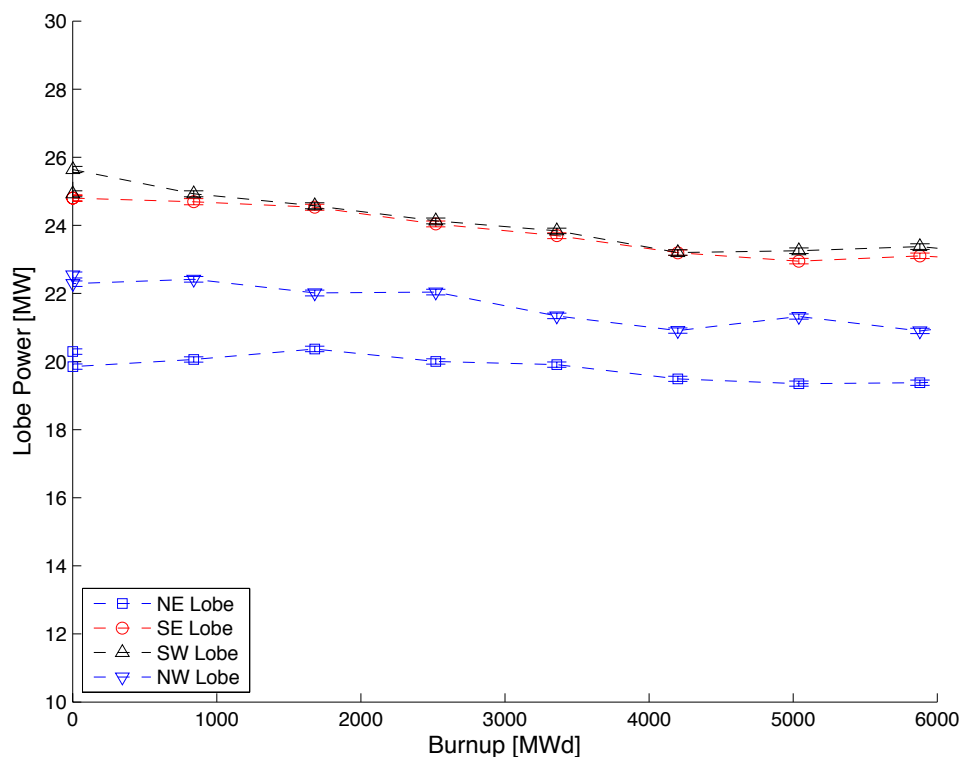


Figure 5.13: Lobe powers over one 56-day cycle

5.6 Further Model Characterization

5.6.1 Model 1 Pin Power Analysis

Figure 5.14 presents power per rod for $1/8^{\text{th}}$ of the core of Model 1, elements 1 through 5, located on the northern side of the northwest flux trap. Power per rod was determined via fission energy deposition and the calculations were performed using 60000 histories per generation for 500 active generations. Element 1 (at the bottom of the graphic) has overall more energy deposition (element power), as it is closer to the

center of the core. The tabulated form of the rod powers within the elements may be found in Appendix D, section 12.6.

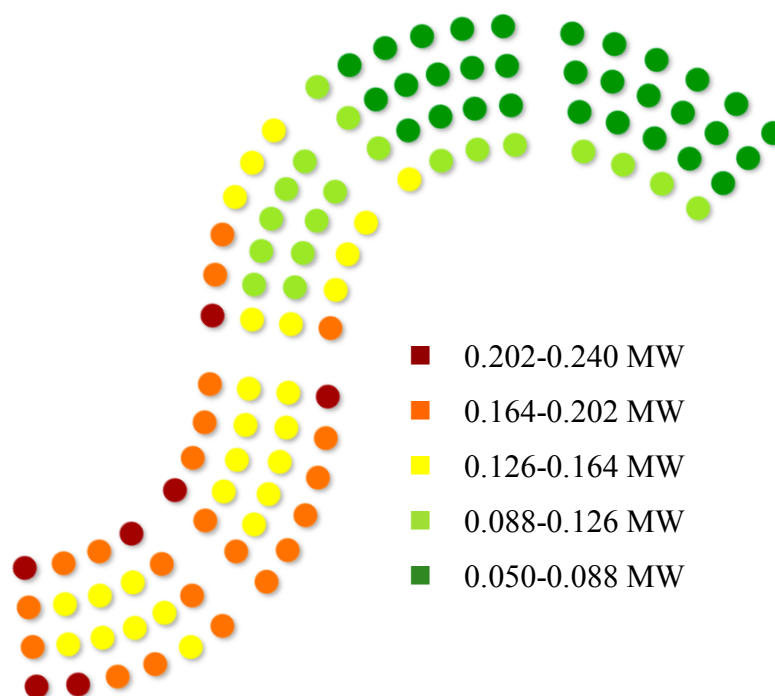


Figure 5.14: Power per rod for elements 1-5 for Model 1

The axial (Figure 5.15) and radial (Figure 5.16) power profiles were generated from the hottest rod, rod 16 of element 1, which is the rod nearest the bottom left corner of Figure 5.14. The axial profile was compared to that of the hottest plate for the HEU 94CIC model. The profiles are presented as power factors. Power factor normalizes the power distribution between the local power and the average power the rod generates.

The axial profile distribution yields an overall trend of the characteristic chopped cosine; more fission events occur in the axial center of the core and taper toward the

top and bottom. As mentioned earlier, the ATR does not have skewed axial power profiles due to the reactivity regulation occurring with either OSCC rotation or fully inserted/withdrawn shims.

The radial power profile of the TRIGA[®] model (Model 1), shown from the centerline out to the edge, illustrates self-shielding of the fuel rods, with more fissions occurring toward the outer radii of the rod. The increase in local power moving toward the outer edge of the rod is due to self-shielding effects within the fuel rod itself.

The values and error analysis associated with these results can be found in Appendix D, section 12.6.

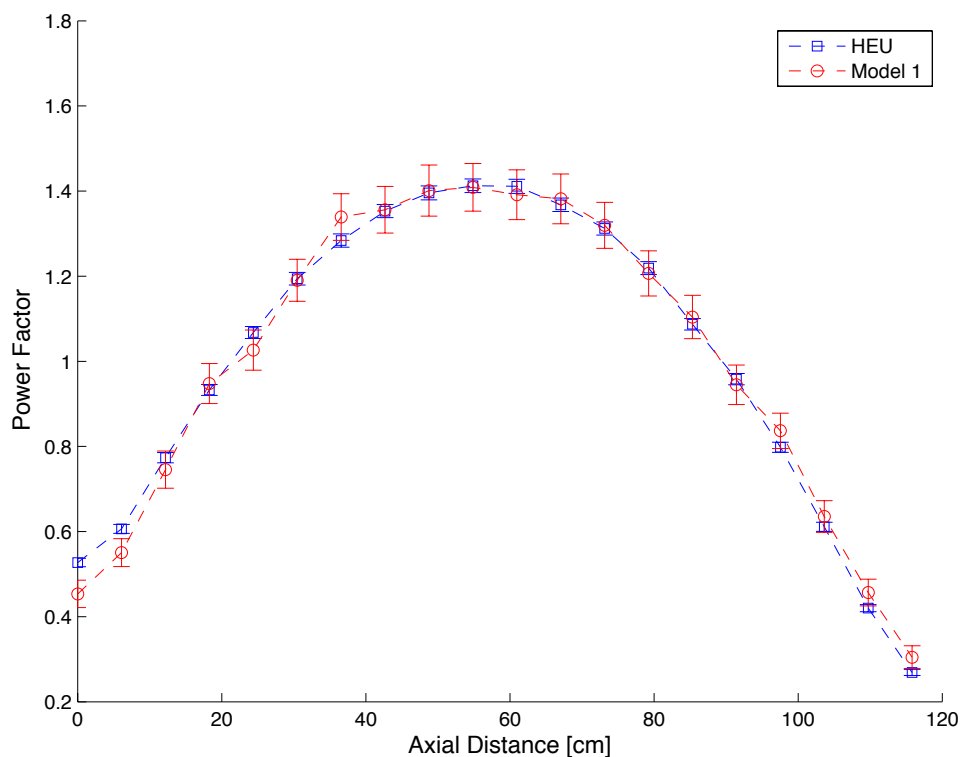


Figure 5.15: Axial power profile for the hottest rod, rod 16 in element 1

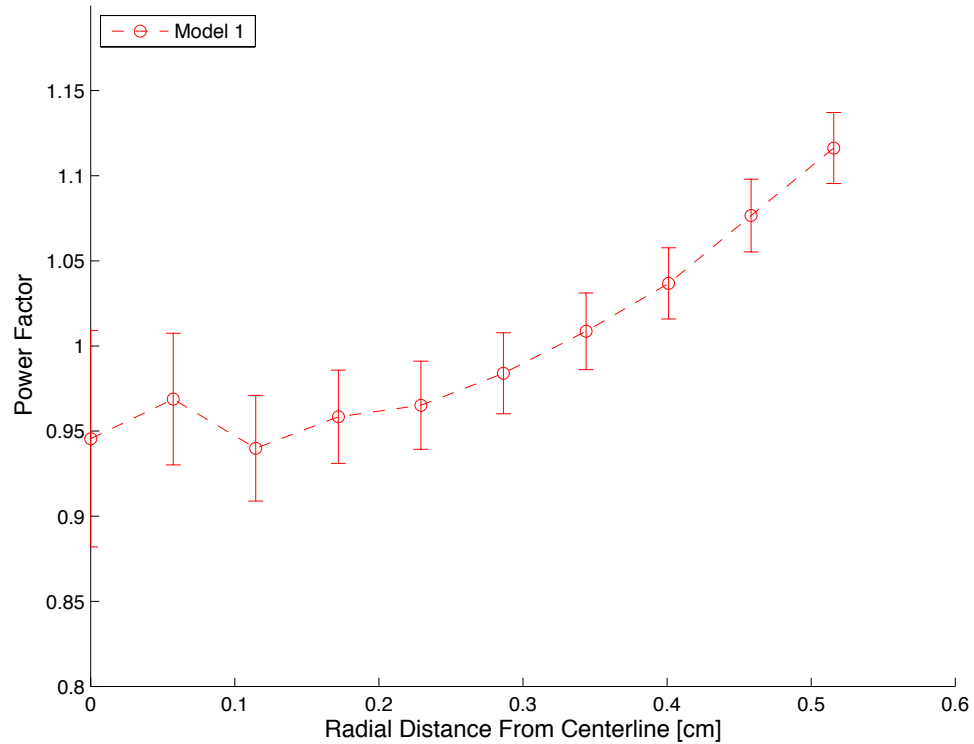


Figure 5.16: Radial power profile for the hottest rod, rod 16 in element 1

5.6.2 Effective Delayed Neutron Fraction & Mean Neutron Generation Time

The effective delayed neutron fraction for the TRIGA[®] Model 1 has a maximum change of -5.00% from the HEU 94CIC model and -6.04% change in the mean neutron generation time from the HEU model to the TRIGA[®] Model 1 over the course of a 56-day cycle, shown in Figure 5.17 and Figure 5.18 and tabulated in Table 5.5. The effective delayed neutron fraction stays constant within uncertainty over the 56-day cycle. The change across the 56-day cycle for Λ , while minimal, mirrors the behavior seen in the reactivity trend over the cycle which can be shown in equation 5.1, where l is the prompt neutron generation time and k is the multiplication factor.

$$\Lambda = \frac{l}{k} \quad 5.1$$

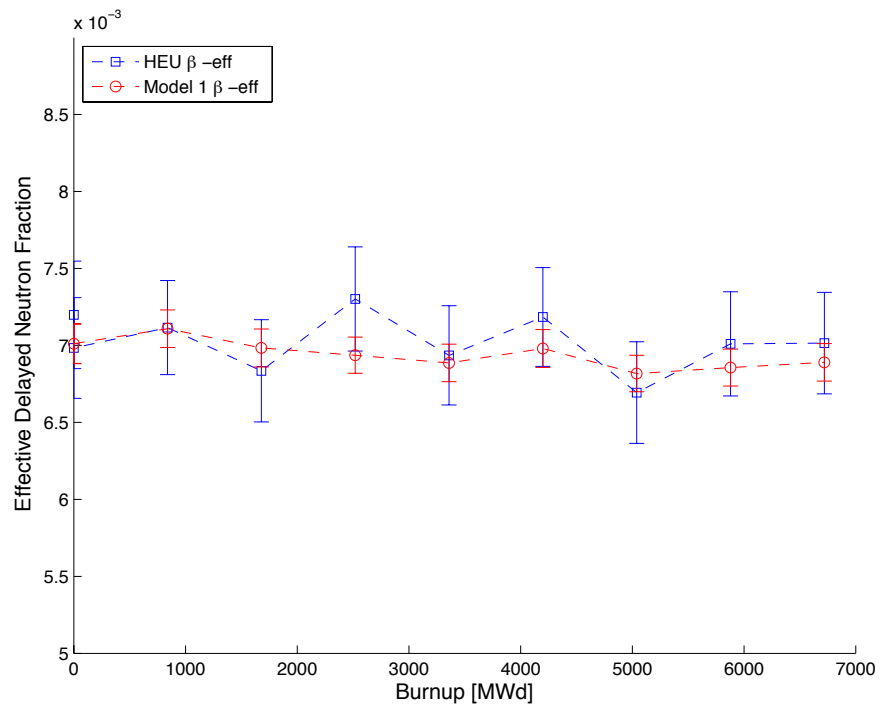


Figure 5.17: Effective delayed neutron fraction over one cycle

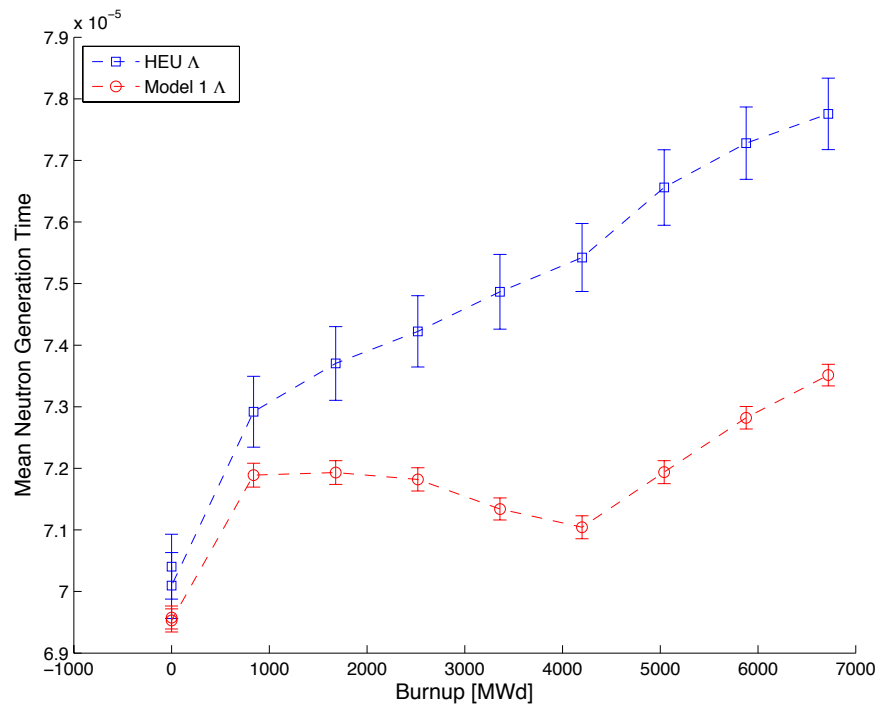


Figure 5.18: Mean neutron generation time over one cycle

Table 5.5: Effective delayed neutron fraction and mean neutron generation time

Burnup [MWd]	β_{eff}			Λ		
	HEU	Model 1	Change [%]	HEU	Model 1	Change [%]
0	7.20E-03	7.01E-03	-2.60	7.04E-05	6.96E-05	-1.17
1.2	6.98E-03	7.01E-03	0.40	7.01E-05	6.95E-05	-0.81
840	7.12E-03	7.11E-03	-0.10	7.29E-05	7.19E-05	-1.41
1680	6.84E-03	6.98E-03	2.17	7.37E-05	7.19E-05	-2.40
2520	7.30E-03	6.94E-03	-5.00	7.42E-05	7.18E-05	-3.24
3360	6.94E-03	6.89E-03	-0.71	7.49E-05	7.13E-05	-4.71
4200	7.18E-03	6.98E-03	-2.84	7.54E-05	7.10E-05	-5.81
5040	6.69E-03	6.82E-03	1.85	7.66E-05	7.19E-05	-6.04
5880	7.01E-03	6.86E-03	-2.19	7.73E-05	7.28E-05	-5.77
6720	7.01E-03	6.89E-03	-1.77	7.78E-05	7.35E-05	-5.46

6 CONCLUSIONS

6.1 Concluding Remarks

A reactor physics study was performed on the Idaho National Laboratory's Advanced Test Reactor. The purpose of this study was to stipulate the feasibility of converting the ATR from its current HEU plate-type fuel to a conceptual LEU TRIGA[®] type fuel. Numerous fuel loading analyses were conducted and provided essential data required to narrow down a feasible model. Not only did these analyses provide insight into which fuel loadings yield the most promising characteristics, they also aided in narrowing down the selection of a specific material and geometric configuration until it was clear that (of the configurations considered herein) Model 1 was the most feasible option. Removing fuel pins relative to the configuration in Model 1 resulted in a more significant rate of depletion, impacting the ATR's ability to maintain its critical state. These models explicitly confirm intuition – rod placement within the fuel envelope is paramount to maintaining a functional reactor configuration. Though there were initially six models to be analyzed, only one LEU TRIGA[®] model posed sufficient potential beyond initial depletion calculations for further analysis. The following conclusions were drawn for the LEU 35/20 TRIGA[®] Model 1 when compared against the functional requirements set forth by Naval Reactors:

- **56-day Cycle Length** – Model 1, with the 35/20 fuel loading, demonstrated the most potential and was burned in such a way so as to mitigate a steep burnup. This allowed the OSCCs to compensate and maintain a 56-day, 120 MW cycle.
- **Specific Fission Rate** – Model 1 met the minimum requirement of $4.8E14$ fissions/s/g of ^{235}U and had a -7.91% change in the SE IPT and a -13.06% change in the SW IPT.
- **Flux Levels and Ratio** – There was a larger than acceptable variation in the fast to thermal flux ratios, within the NW flux trap. The fast and thermal flux values obtained for the nine core locations also had large variations between 8.93% and 18.17%.

- **Lobe Power** – The corner lobe powers varied by as much as 3.32% over the course of a 56-day cycle.
- **Power Density** – The power per rod values, presented in Figure 5.14 could prove to be acceptable when compared against the abundant level of forced convective flow through the ATR core and acceptable heat fluxes that TRIGA® fuel experiences in open pool type reactors [41].
- **Reactor Physics Parameters** – The effective delayed neutron fraction was found to be constant within uncertainty over a 56-day cycle. The mean neutron generation decreased by as much as 6.04% in the TRIGA® Model 1, but overall had a minimal change over the cycle.

While several of the analyzed parameters were outside the bounds of the Naval Reactors program functional requirements for the ATR, this study had several optimistic results that justify further analysis, which, if performed, may indicate that this otherwise unlikely option for the ATR conversion with TRIGA® fuel is viable.

6.2 Future Work

The minimum functional requirements delineated by the Naval Reactors program only specify requirements for one 56-day cycle. As a result, this study was performed without core shuffling or refueling and further study could consider at a cycle length beyond 56 days, adding a depletion analysis of a prototypic mixed core containing fresh, once burned, and twice burned fuel.

Further study could also consider be a thermal hydraulic analysis in order to better understand the impact of the 3:1 power tilt and expand the preliminary power analysis done here.

An additional assumption made as a part of this study was the selection of stainless steel cladding material in contrast to a potentially viable alternative option (aluminum). The switch to stainless steel cladding resulted in only a very small

difference in k_{eff} , but there could possibly be more serious ramifications such as core reloading and reactor operation delays due to the longer lived half-lives in activated stainless steel. Further investigation toward the programmatic impact of implementing stainless steel cladding is recommended if TRIGA[®] fuel is studied further. Additional analysis with regards to cladding material should be done in order to determine if the results from models with stainless steel cladding is representative of results from models with Incoloy cladding, as the results in Appendix B, section 10.2 suggest.

Lastly, if potential further analysis of the TRIGA[®] fuel design leads to a model that meets the minimum functional requirements set by the Naval Reactors Program, then a formal benchmark study would need to be conducted against an independent reactor physics code.

7 BIBLIOGRAPHY

- [1] Argonne National Laboratory. (2012, January) Reduced Enrichment for Research and Test Reactors. [Online]. <http://rertr.anl.gov/>
- [2] International Atomic Energy Agency. (2011, February) IAEA Welcomes US New Global Threat Reduction Initiative. [Online]. http://www.iaea.org/newscenter/news/2004/gtri_initiative.html
- [3] Clifford J. Stanley and Frances M. Marshall, "Advanced Test Reactor- A National Scientific User," in *Proceedings of the 16th International Conference on Nuclear Engineering*, Orlando, FL, 2008.
- [4] Idaho National Laboratory, "Upgraded Final Safety Analysis Report for Advanced Test Reactor," UFSAR SAR-153, 2006.
- [5] D.M Wachs, "RERTR Fuel Development and Qualification Plan," Idaho National Laboratory, INL/EXT-05-01017, 2007.
- [6] P. Lemoine and D Wachs, "High Density Fuel Development for Research Reactors," in *Reduced Enrichment for Research and Test Reactors Meeting*, Czech Republic, 2007, pp. 1-15.
- [7] AP Cochran, Naval Reactors Functional Requirements for the Advanced Test Reactor, December 11, 2008, NR:RM:APCochran S#08-04461.
- [8] Mark DeHart, "Physics Analysis of the Enhanced LEU Fuel (ELF) Design," Idaho National Laboratory, ECAR ECAR-2202,.
- [9] Michael A. Pope, "Physics Analysis of the Integral Side Plate Burnable Absorber - Cadmium Wire Fuel Design," Idaho National Laboratory, ECAR ECAR-2174, 2013.
- [10] Mark DeHart, "Physics Analysis of the Integral Side Plate Burnable Absorber - Boron Fuel Design," Idaho National Laboratory, ECAR ECAR-2140, 2013.
- [11] M. Asgari, B. Forget, S. Piet, R. Ferrer, and S. Bays, "Computational Neutronic Methods and Transmutation Performance Analyses for Light Water Reactors," Idaho National Laboratory, External Report INL/EXT-07-12472, 2007.

- [12] G.S. Chang, R.G. Ambrosek, and M.A. Lillo, "Advanced Test Reactor LEU Fuel Conversion Feasibility Study," Idaho National Laboratory, Annual Report INL/EXT-06-11887, 2006.
- [13] G.S. Chang, R.G. Ambrosek, and M.A. Lillo, "Advanced Test Reactor LEU Fuel Conversion Feasibility Study," in *The RERTR-2005 International Meeting on Reduced Enrichment for Research and Test Reactors*, Boston, MA, 2005.
- [14] Mark DeHart and Gray S. Chang, "Evaluation of Core Physics Analysis Methods for Conversion of the INL Advanced Test Reactor to Low-Enrichment Fuel," in *PHYSOR 2012*, Knoxville, TN, 2012.
- [15] Jaakko Leppänen and Maria Pusa, "Burnup Calculation Capability in the PSG2 / Serpent Monte Carlo Reactor Physics Code," in *International Conference on Mathematics, Computational Methods & Reactor Physics*, Saratoga Springs, NY, 2009.
- [16] Jaakko Leppänen, "A New Assembly-Level Monte Carlo Neutron Transport Code For Reactor Physics Calculations," in *Mathematics and Computation, Supercomputing, Reactor Physics and Nuclear and Biological Applications*, Palais des Papes, Avignon, France, 2005.
- [17] David W. Nigg et al., "Improved Computational Neutronics Methods and Validation Protocols for the Advanced Test Reactor," in *PHYSOR*, Knoxville, TN, 2012.
- [18] D.S. Lucas et al., "Comparison Of The 3-D Deterministic Neutron Transport Code Attila® To Measure Data, MCNP And MCNPX For The Advanced Test Reactor," Idaho National Laboratory, M&C 2005 International Topical Preprint INL/CON-05-00662, 2005.
- [19] Jaakko Leppänen, Development of a New Monte Carlo Reactor Physics Code, June 2007.
- [20] James J. Duderstadt and Louis J. Hamilton, *Nuclear Reactor Analysis*.: John Wiley & Sons, 1976.
- [21] Jaakko Leppänen, "Performance of Woodcock delta-tracking in lattice physics

- applications using the Serpent Monte Carlo reactor physics burnup calculation code," *Annals of Nuclear Energy*, vol. 37, pp. 715-722, 2010.
- [22] R Macian, M Zimmerman, and R Chawla, "Assessment of CASMO-4 Predictions of the Isotopic Inventory of High Burn-up MOX Fuel," in *PHYSOR*, Chicago, 2004.
- [23] E Bomboni, N Cerullo, E Fridman, G Lomonaco, and E Shwageraus, "Comparison Among MCNP-Based Depletion Codes Applied to Burnup Calculations of Pebble-Bed HTR Lattices," *Nuclear Engineering and Design*, vol. 240, pp. 918-924, 2010.
- [24] Jaakko Leppänen, Serpent Monte Carlo Neutron Transport Code, April 30, 2012.
- [25] D.D. Keiser Jr., S.L. Hayes, M.K. Meyer, and C.R. Clark, "High Density, Low-Enriched Uranium Fuel for Nuclear Research Reactors," *JOM*, vol. 55, no. 9, pp. 55-58, September 2003.
- [26] R.B. Pond, N.A. Hanan, and J.E. Matos, "LEU Conversion Feasibility Studies for the BMRR and HFBR," in *ANS Winter Meeting and Embedded Topical Meetings*, Albuquerque, New Mexico, 1997.
- [27] R.J. Ellis, J.C. Gehin, and R.T. Primm, "Cross Section Generation and Physics Modeling in a Feasibility Study of the Conversion of the High Flux Isotope Reactor Core to Use Low-Enriched Uranium Fuel," Oak Ridge National Laboratory, 2006.
- [28] A.L. Hanson and D.J. Diamond, "Calculation of Design Parameters for an Equilibrium LEU Core in the NBSR," Brookhaven National Laboratory, BNL-96386-2011-IR, 2011.
- [29] J. Charles McKibben, Kiratadas Kutikkad, and Leslie P. Foyto, "Current Status of the Missouri University Research Reactor HEU to LEU Conversion Feasibility Study," in *International RERTR Meeting*, Cape Town, Republic of South Africa, 2006.
- [30] Thomas H. Newton, Erik H. Wilson, A Bergeron, N. Horelik, and Stevens, J.G. , "Neutronic Analyses for HEU to LEU Fuel Conversion of the Massachusetts

- Institute of Technology MITR Reactor," Argonne National Laboratory, ANL/RERTR/TM-10-40, 2010.
- [31] John G. Stevens, Technical Challenges for Conversion of U.S. High-Performance Research Reactors (USHPRR), November 29, 2010, Argonne National Laboratory.
- [32] Michael Pope, "Physics Analysis of the Integral Side Plate Burnable Absorber-Cadmium Wire Fuel Design," Idaho National Laboratory, ECAR ECAR-2174,.
- [33] Frances M. Marshall, "Advanced Test Reactor Capabilities and Future Operating Plans," Idaho National Laboratory,.
- [34] Wade Marcum, Predicting Mechanical Instability of a Cylindrical Plate under Axial Flow Conditions, 2010.
- [35] Mark D. DeHart, "Conceptual LEU Fuel Design for ATR Using Hafnium Poisoning," Idaho National Laboratory, ECAR CDR-107, 2012.
- [36] C Ellis, J Bolin, and J Saurwein, "Scoping Study of LEU UZrH Fuel as a Replacement Fuel for the Massachusetts Institute of Technology Research Reactor (MITR)," General Atomics, 39293R00006,.
- [37] U.S. Nuclear Regulatory Commission, "Safety Evaluation Report on High-Uranium Content, Low-Enriched Uranium-Zirconium Hydride Fuels for TRIGA Reactors," NUREG-1282, 1987.
- [38] Wade R. Marcum, Thermal Hydraulic Analysis of the Oregon State TRIGA Reactor Using RELAP5-3D, 2008.
- [39] International Atomic Energy Agency, "Generic Procedures for Response to a Nuclear or Radiological Emergency at Triga Research Reactors," Vienna, 2011.
- [40] Idaho National Laboratory, "Updated Final Safety Report," Advanced Test Reactor, Sec. 4.3.1.5.2,.
- [41] W.R. Marcum et al., "Steady-State Thermal-Hydraulic Analysis of the Oregon State University TRIGA Reactor Using RELAP5-3D," *Nuclear Science and Engineering*, vol. 162, pp. 261-274, 2009.
- [42] MT Simnad, "The U-ZrHx Alloy: Its Properties and Use in TRIGA Fuel,"

General Atomics, GA Project No. 4314, 1989.

- [43] W. R. Marcum et al., "A Comparison of Pulsing Characteristics of the Oregon State University TRIGA Reactor with FLIP and LEU Fuel," *Nuclear Science and Engineering*, no. 171, pp. 150-164, 2012.
- [44] Tetsuo Matsumoto and Nobuhiro Hayakawa, "Benchmark Analysis of TRIGA Mark II Reactivity Experiment Using a Continuous Energy Monte Carlo Code MCNP," *Nuclear Science and Technology*, vol. 37, no. 12, pp. 1082-1087, December 2000.

8 NOMENCLATURE

Acronyms

94CIC	1994 Core Internals Change-out
ATR	Advanced Test Reactor
BOL	Beginning of Life
DoE	Department of Energy
FD	Fuels Development
GTRI	Global Threat Reduction Initiative
HEU	Highly Enriched Uranium
HFBR	High Flux Beam Reactor
HFIR	High Flux Isotope Reactor
HPRR	High Performance Research Reactor
INL	Idaho National Laboratory
IPT	In-Pile Tube
LEU	Low Enriched Uranium
MCNP	Monte Carlo N-Particle
MITR	Massachusetts Institute of Technology Reactor
MURR	University of Missouri Columbia Research Reactor
NBSR	National Bureau of Standards Reactor
NR	Naval Reactors
NRC	Nuclear Regulatory Commission
OSCC	Outer Shim Control Cylinder
OSTR	Oregon State TRIGA [®] Reactor
ORIGEN	Oak Ridge Isotope Generation and Depletion code
RERTR	Reduced Enrichment for Research and Test Reactors
SCALE	Standardized Computer Analyses for Licensing Evaluation
TRIGA	Training Research Isotope General Atomic

Variables

σ	Error
n	Number of fuel rods
PF	Power Factor
P	Power
s	Number of segments in the power distribution

APPENDIX

9 APPENDIX A: SENSITIVITY STUDY ON H/ZR RATIO

When fabricating fuel, there are tolerances for all compositions and dimensions that are dictated by fuel performance characteristics and the manufacturer's capabilities, which is why it is important to investigate the effects that these tolerances may have on the fuel. The data presented in Figure 9.1, calculated with 5000 histories per generation for 500 generations, is a preliminary sensitivity analysis of the effects of the ratio of hydrogen to zirconium in the UZrH TRIGA[®] fuel. The nominal ratio of hydrogen to zirconium in TRIGA fuel is 1.60 [37]. The upper limit of this ratio is 1.65; this comes from the internal pressure that results from hydrogen dissociation, which is heavily dependent on the hydrogen-zirconium ratio. This pressure leads to stress on the cladding that affects the upper limit of the fuel temperature [42]. The lower limit in this sensitivity analysis was taken from the data sheets for the most recent fuel shipment received by the OSTR, as stated by Steve Reese, director of the Oregon State Radiation Center.

The slight increase in reactivity due to the overall increase in the amount of hydrogen can be attributed to neutron energy loss, thermalization, caused by elastic scattering events. This increase in reactivity shows that the H/Zr ratio, within license tolerances, can have a significant impact on core lifetime.

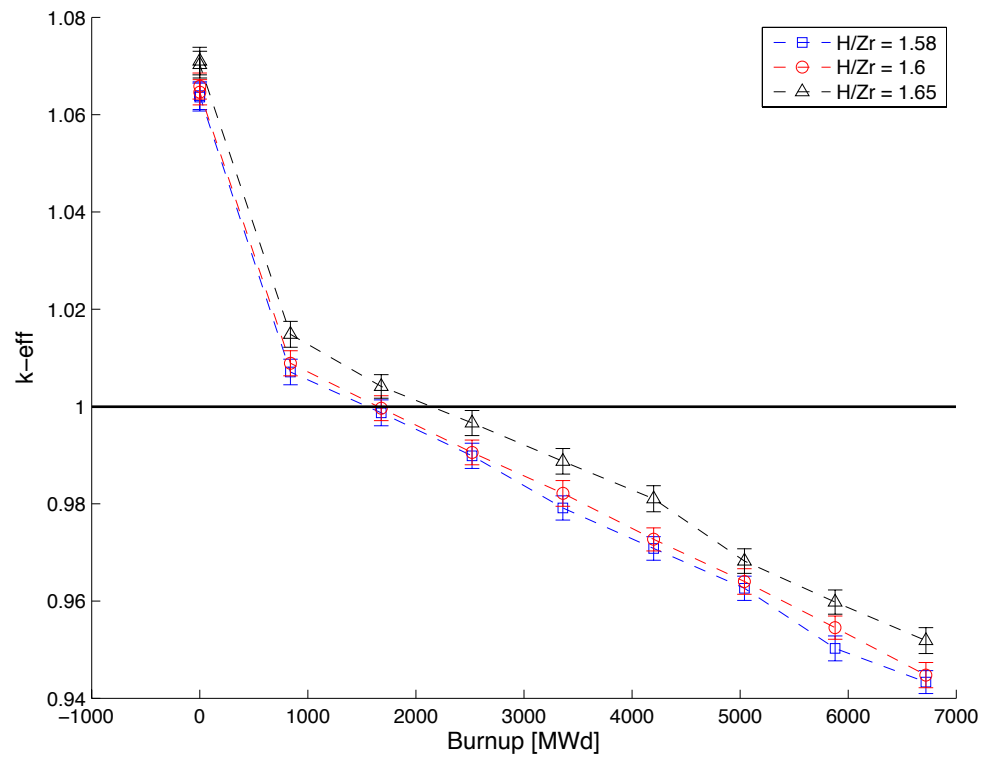


Figure 9.1: The effects of the H/Zr ratio over one 56-day, 120 MW cycle

10 APPENDIX B: OTHER TRIGA[®] COMPOSITIONS

The 35/20 TRIGA[®] fuel analysis was obtained through systematically eliminating the other potential fuel compositions tabulated in Table 4.2. The methodologies and logic used to justify the further analysis of the 35/20 fuel are expounded here.

10.1 30/20 TRIGA[®] Fuel

The reactivity vs. OSCC rotation plot is shown in Figure 10.1 (obtained at BOL using 1000 histories per generation for 500 generation). The shape of these plots results from the change in orientation of the OSCCs. The hafnium within the OSCCs yields the largest solid angle potential toward the fissile material given a 0° rotation; as each OSCC is rotated away from the core, the differential reactivity worth is maximum near a rotation angle of approximately 90° rotation as this is the relative location where the largest change in hafnium material is exposed to the core given a differential rotation angle. As the OSCCs rotate away from the core, a larger surface area of hafnium is exposed to the core, however, the hafnium is farther from the fissile material and shielded by the rotation drum resulting in a much smaller differential worth. The OSCCs have less worth for all of the TRIGA[®] models, particularly for Model 2, 3, and 4. These three models all have larger gaps of water between the fuel and the OSCCs. These regions of water are a source of thermalized neutrons and placing this source between the fuel and the absorbent hafnium of the OSCCs enabling more absorption by the OSCCs, furthermore, these models have less fissile material that is comprised within the core region than all other models. Additionally, this plot shows that none of the models were capable of reaching critical even at BOL except Model 1, Model 5 and Model 6. Model 5 was eliminated due to its rapid rate of burnup that results from having the least amount of fissile material available. Model 5 exhibits a unique burnup, which yields promising k_{eff} values near the beginning of the first 56-day cycle. However, Model 5 exhibits a rapid burnup rate and ultimately drops into a subcritical state shortly after initial startup. This unique behavior of Model 5 is likely due to the large water regions in the center of each element that provide significantly more opportunity for neutron thermalization and subsequent fissions than most other

models. Model 6 obtains criticality only for a very limited rotation range and will not be able to sustain criticality through burnup.

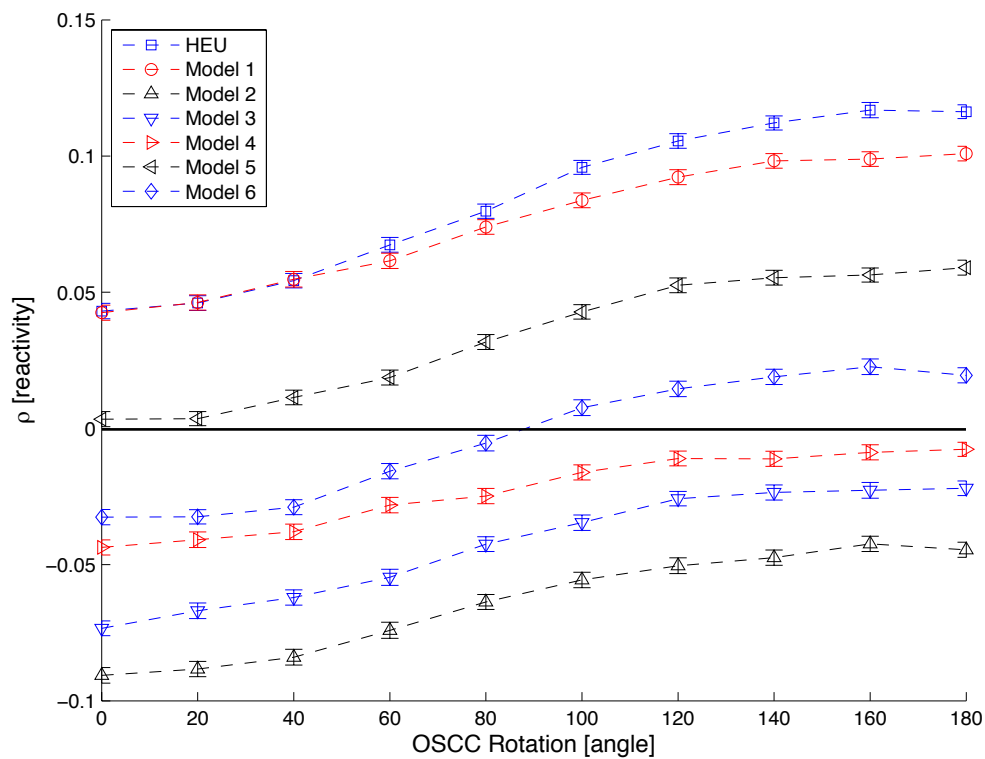


Figure 10.1: Reactivity vs. OSCC rotation angle for the 30/20 TRIGA fuel

The burnup trend established in Figure 10.2 shows that the steep trend exhibited by Model 1 will not enable a critical state by the end of the cycle, even with all neck shims removed (as is shown here).

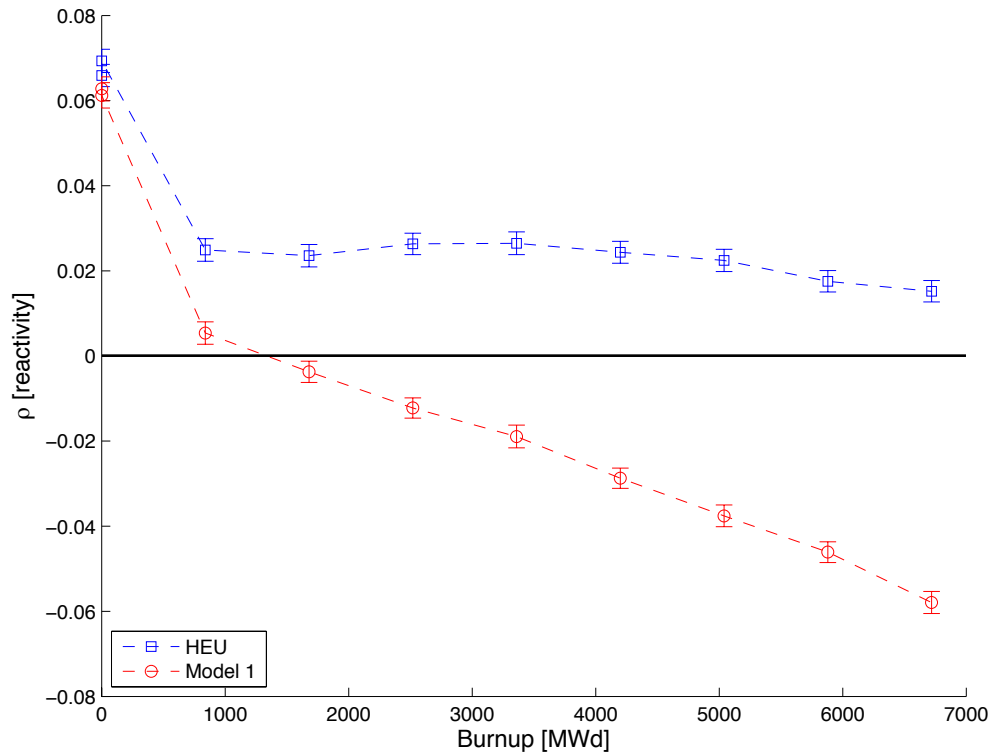


Figure 10.2: Burnup for the 30/20 loaded Model 1 and the HEU model

The 30/20 TRIGA[®] fuel composition, with all neck shims out and the OSCC rotation at 180°, ensuring a maximum positive reactivity insertion, lasts up to 35 days at 120 MW with Model 1.

Figure 10.3 presents the OSCC rotation necessary to maintain a k_{eff} of unity for each depletion step for the first 56-day, 120 MW cycle. This plot was obtained by calculating the decrease in reactivity over the first burnup cycle and finding what angle the OSCCs need to be positioned at to compensate using the data from Figure 10.1 and Figure 10.2. The worth of the OSCCs decrease with burnup, so the cycle length shown in Figure 10.3 is actually an over-estimate of how long Model 1 could last.

The inability of the 30/20 model with the most fissile material to reach the end of a 56-day cycle indicated that the other models with this fuel composition would also be unsuccessful and warranted moving on to models with larger fuel loadings.

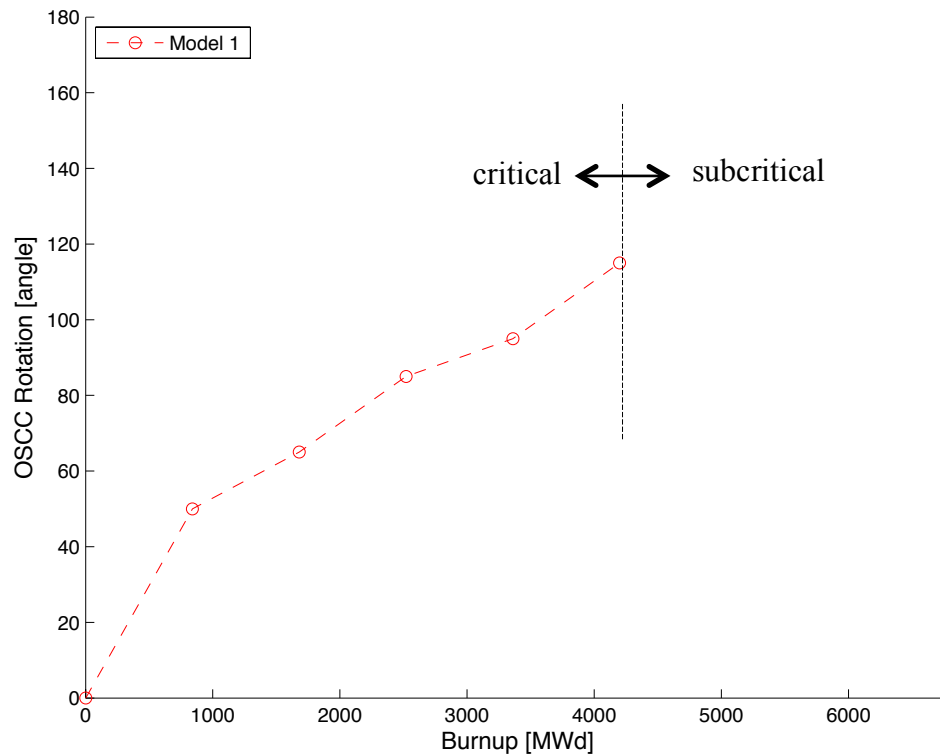


Figure 10.3: OSCC rotation vs. MWd for Model 1 fueled with 30/20 TRIGA fuel

10.2 45/20 TRIGA[®] Fuel

After the 30/20 fuel proved to be insufficient, the 45/20 fuel composition, with both stainless steel cladding and Incoloy cladding was investigated with 5000 histories per generation for 500 active generations. The initial results that included the Incoloy cladding showed a substantial decrease in the reactivity, and was not applied to any other model. However, after attempting to account for this drop in reactivity, it was discovered that the reference used for the Incoloy composition [36] misrepresented the units of the composition. The corrected composition, shown in Figure 10.4, shows that

the stainless steel-clad models may be representative of results obtained using Incoloy cladding.

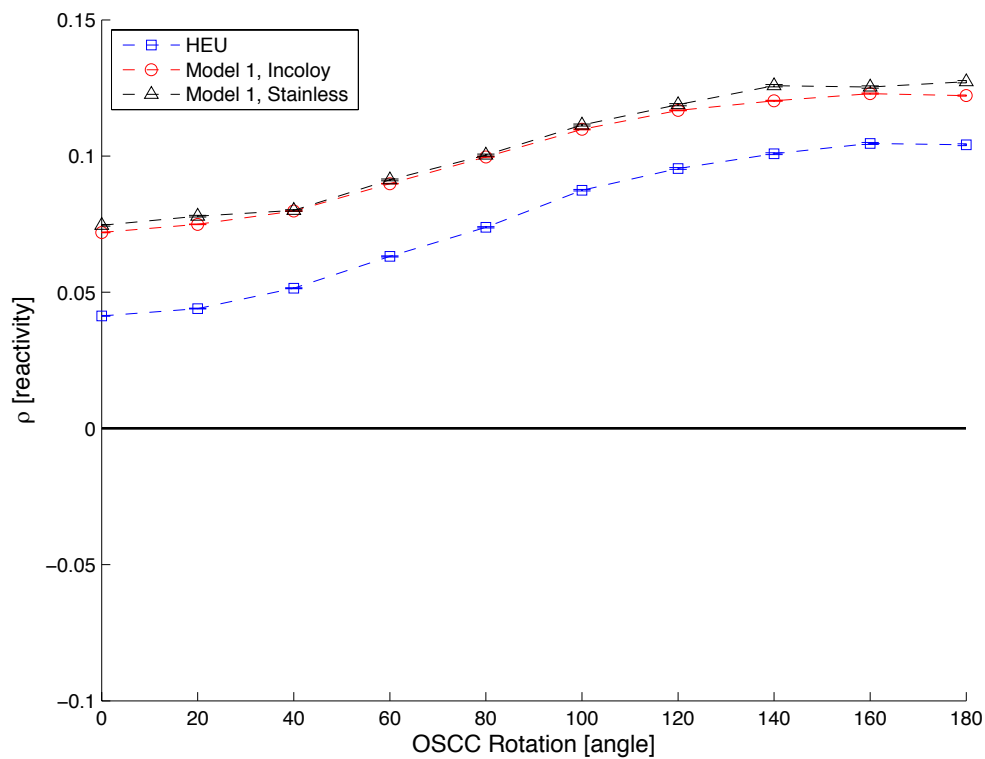


Figure 10.4: Reactivity vs. OSCC rotation with Incoloy and stainless steel cladding

The 45/20 fuel composition with the stainless steel cladding resulted in a supercritical core at BOL, a k_{eff} of 1.012 ± 0.0013 , with all neck shims inserted and the OSCCs rotated to 0° . While the burnup rate looked promising, see Figure 10.5, the reactivity of the cold, clean core before the xenon drop is too high.

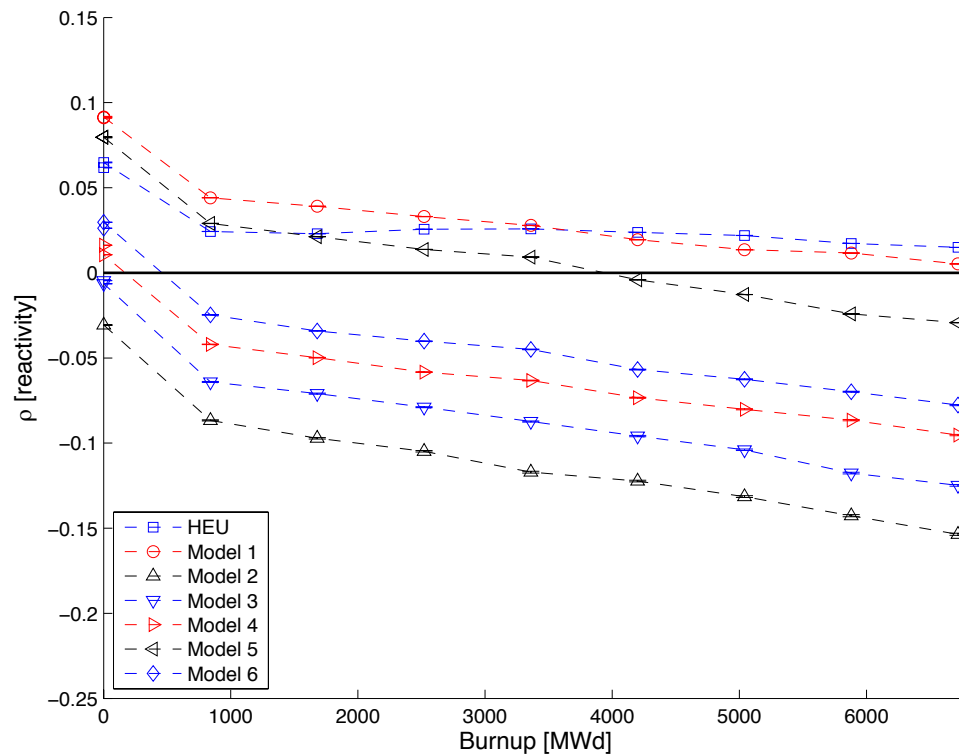


Figure 10.5: Burnup for the 45/20 TRIGA fuel

The remaining TRIGA[®] models aside from Model 5, do not last the 56 day cycle, as shown in Figure 10.6, even with all of the neck shims removed. Model 5, with some neck shim maneuvering could potentially last the entire 56 day cycle without being supercritical at the beginning, but analysis shows that for an OSCC rotation angle of 0° and all neck shims inserted, Model 5 has a $k_{eff} = 0.9996 \pm 0.0024$, which provides no shutdown margin. Additionally, Model 5 has a specific fission rate in the SW IPT of $4.76E14 \pm 2.59E12$, which does not meet the minimum functional requirement of $4.8E14$. For these reasons, Model 5 is eliminated from further analysis.

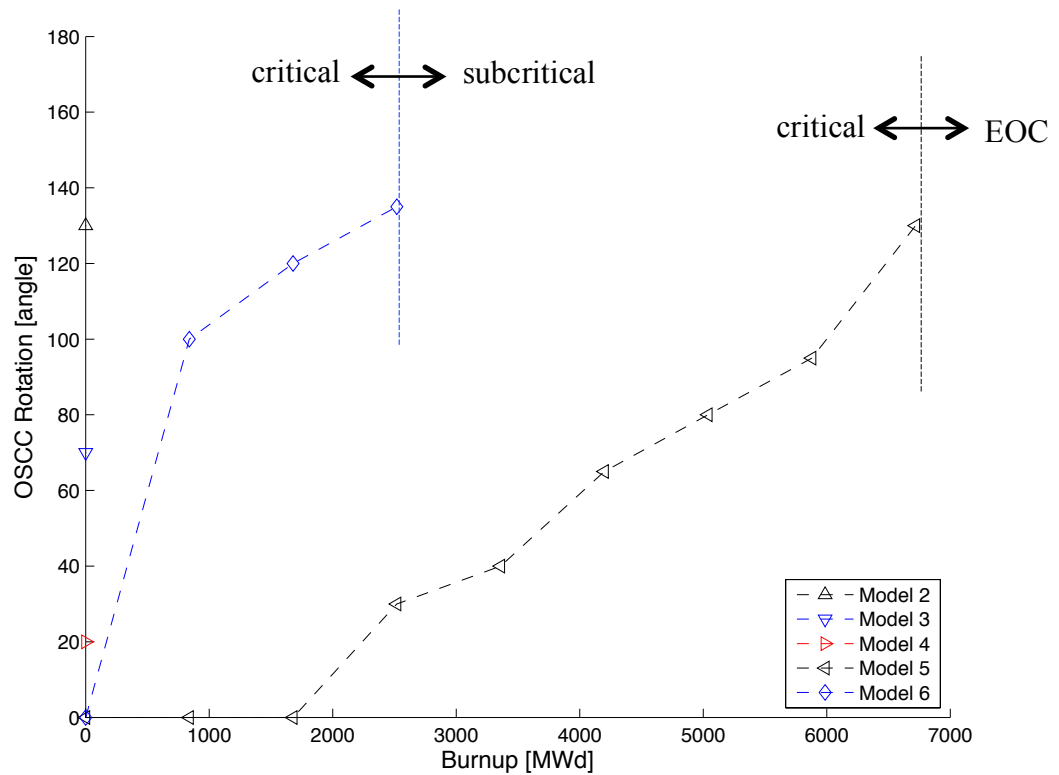


Figure 10.6: OSCC rotation vs. MWd for the 45/20 TRIGA fuel

10.3 40/20 TRIGA[®] Fuel

The 40/20 TRIGA[®] fuel, calculated with the same number of histories and generations, had the same issue as the 45/20 fuel: too much reactivity at the beginning of life and not enough reactor shutdown margin. After Model 1 was shown to have a k_{eff} of 1.00500 ± 0.00276 , with all 24 neck shims inserted and the OSCCs rotated to 0° , the 40/20 TRIGA[®] fuel was not analyzed further.

11 APPENDIX C: VARIED BURN REGIONS

When performing any numerical analysis, the resolution of the computational domain (grid resolution) can significantly impact numerical diffusion and thus the accuracy of the results. One potential concern in this capacity is the fuel rods' geometric resolution when performing depletion calculations. Because of the cylindrical rod geometry, self-shielding has been shown (seen in Figure 5.16) to impact the radial power distribution within each rod and thus the local fission rate, which in turn impacts the local rate of burnup within each rod. For the depletion calculation done for the OSTR, three annular burn regions were used. In order to confirm the results produced for a rod having three discrete radial sections are valid here, a sensitivity study was performed. Using 30/20 fueled Model 1, a depletion calculation was run over a 56-day, 120 MW cycle. Three different simulations were run; one simulation contained a single radial zone within the fuel rod, the second contained three radial zones, and the last contained five. Figure 11.1 presents the value of k_{eff} over the 56-day cycle for each of these simulations. As seen from Figure 11.1, no discernible impact of k_{eff} was found between the three different models, lending credibility to the depletion calculations performed.

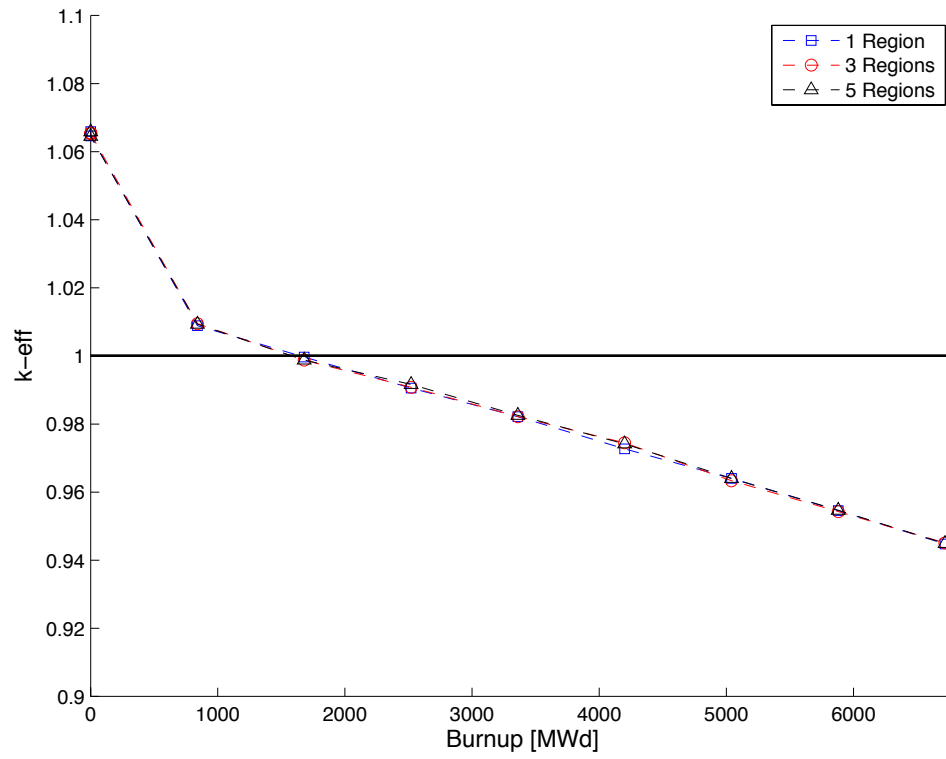


Figure 11.1: The varied burn regions for the TRIGA[®] fuel

12 APPENDIX D: TABULATED VALUES, STATISTICAL ERROR, AND ERROR ANALYSIS

12.1 Depletion Values and Percent Error

The error for each ρ value over the course of the depletion calculation was obtained from the output file by propagating the error from k_{eff} according to equation 12.1 and is presented in Table 12.1 as the percent error with a 2σ confidence interval.

$$\sigma_{\rho} = \frac{k_{eff}-1}{k_{eff}} \sqrt{2 * \left(\left(\frac{\sigma_{k_{eff}}}{k_{eff}} \right)^2 + \left(\frac{\sigma_{k_{eff}}}{k_{eff}} \right)^2 \right)} \quad 12.1$$

Table 12.1: The ρ values and the percent error over burnup

Burnup [MWd]	HEU 94CIC Model		35/20 TRIGA [®] Model 1	
	ρ	Error [%]	ρ	Error [%]
0	6.18E-02	0.35	2.82E-02	0.28
1.2	6.48E-02	0.36	2.81E-02	0.27
840	2.43E-02	0.36	-1.65E-02	0.29
1680	2.30E-02	0.36	-1.48E-02	0.39
2520	2.57E-02	0.35	-1.50E-02	0.38
3360	2.58E-02	0.37	-1.04E-02	0.38
4200	2.38E-02	0.36	-7.07E-03	0.36
5040	2.19E-02	0.36	-1.44E-02	0.37
5880	1.72E-02	0.35	-2.00E-02	0.38
6720	1.50E-02	0.35	-3.07E-02	0.39

12.2 OSCC Analysis Error Analysis

The error for each ρ value in Table 4.1, obtained from equation 12.1 and equation 12.2, is the percent error with a 2σ confidence interval. For the 0 MWd burnup step,

the 0° rotation angle for the 0-5880 MWd burnup steps, and the 180° rotation angle for the 6720 MWd burnup step the error was obtained from the output file and propagated according to equation 12.1. All other error was propagated according to equation 12.2, where $\sigma_{\rho @ Y MWd, X^\circ}$ is the error for ρ at any given burnup step and rotation angle, $\sigma_{\rho @ 0 MWd, 0^\circ}$ is the error for ρ at 0 MWd and 0°, $\sigma_{\rho @ 0 MWd, X^\circ}$ is the error for ρ at 0 MWd and any given rotation angle, and $\sigma_{\rho @ Y MWd, 0^\circ}$ is the error for ρ at any given burnup step at 0°.

$$\sigma_{\rho @ Y MWd, X^\circ} = \sqrt{\sigma_{\rho @ 0 MWd, 0^\circ}^2 + \sigma_{\rho @ 0 MWd, X^\circ}^2 + \sigma_{\rho @ Y MWd, 0^\circ}^2} \quad 12.2$$

Table 12.2: The ρ values and the percent error for varied OSCC angles and burnup

	0°	20°	40°	60°	80°	100°	120°	140°	160°	180°
0 MWd	1.27E-03	5.79E-03	1.38E-02	2.74E-02	4.19E-02	5.51E-02	6.48E-02	7.09E-02	7.35E-02	7.28E-02
Error (%)	1.24E-01	1.24E-01	1.24E-01	1.33E-01	1.24E-01	1.24E-01	1.19E-01	1.13E-01	1.19E-01	1.16E-01
840 MWd	-3.54E-02	-3.05E-02	-2.19E-02	-7.30E-03	8.25E-03	2.23E-02	3.28E-02	3.93E-02	4.20E-02	4.13E-02
Error (%)	3.79E-01	4.06E-01	4.07E-01	4.10E-01	4.08E-01	4.09E-01	4.07E-01	4.05E-01	4.07E-01	4.06E-01
1680 MWd	-3.20E-02	-2.71E-02	-1.86E-02	-4.10E-03	1.13E-02	2.53E-02	3.58E-02	4.22E-02	4.49E-02	4.42E-02
Error (%)	3.73E-01	4.03E-01	4.03E-01	4.06E-01	4.04E-01	4.05E-01	4.03E-01	4.02E-01	4.04E-01	4.03E-01
2520 MWd	-2.73E-02	-2.25E-02	-1.40E-02	3.31E-04	1.56E-02	2.95E-02	3.98E-02	4.63E-02	4.89E-02	4.82E-02
Error (%)	3.93E-01	4.21E-01	4.22E-01	4.25E-01	4.23E-01	4.23E-01	4.22E-01	4.20E-01	4.22E-01	4.21E-01
3360 MWd	-2.29E-02	-1.81E-02	-9.69E-03	4.54E-03	1.97E-02	3.35E-02	4.37E-02	5.01E-02	5.27E-02	5.21E-02
Error (%)	3.71E-01	4.03E-01	4.03E-01	4.07E-01	4.05E-01	4.05E-01	4.04E-01	4.02E-01	4.04E-01	4.03E-01
4200 MWd	-1.52E-02	-1.06E-02	-2.26E-03	1.18E-02	2.67E-02	4.03E-02	5.04E-02	5.67E-02	5.93E-02	5.86E-02
Error (%)	3.99E-01	4.31E-01	4.31E-01	4.34E-01	4.32E-01	4.33E-01	4.31E-01	4.30E-01	4.32E-01	4.31E-01
5040 MWd	-2.16E-02	-1.68E-02	-8.43E-03	5.76E-03	2.09E-02	3.46E-02	4.48E-02	5.12E-02	5.38E-02	5.32E-02
Error (%)	3.56E-01	3.91E-01	3.91E-01	3.95E-01	3.93E-01	3.93E-01	3.92E-01	3.90E-01	3.92E-01	3.91E-01
5880 MWd	-3.21E-02	-2.73E-02	-1.87E-02	-4.21E-03	1.12E-02	2.52E-02	3.57E-02	4.21E-02	4.48E-02	4.41E-02
Error (%)	3.73E-01	4.03E-01	4.03E-01	4.06E-01	4.04E-01	4.05E-01	4.03E-01	4.02E-01	4.04E-01	4.03E-01
6720 MWd	-6.56E-02	-6.05E-02	-5.13E-02	-3.59E-02	-1.95E-02	-4.59E-03	6.46E-03	1.33E-02	1.62E-02	1.55E-02
Error (%)	3.87E-01	3.88E-01	3.88E-01	3.91E-01	3.89E-01	3.90E-01	3.88E-01	3.86E-01	3.88E-01	3.39E-01

12.3 Specific Fission Rate Error Analysis

The relative statistical error for the fissions/s was available directly from the Serpent output file; this error, converted to absolute error, was divided by 24 inches since the

experiment cylinder has 1 g/in, which gave the absolute error of the specific fission rate in fissions/s/g. The absolute error of the specific fission rate was then divided by the lobe power and then multiplied by 60 MW to reflect the renormalization of the fission rate per gram. These values are tabulated in Table 12.3.

Table 12.3: Error associated with the fission/s/g for each lobe

Flux Trap	HEU 94CIC Model		35/20 TRIGA [®] Model 1	
SW	5.55E+14	±0.50%	4.83E+14	±0.54%
SE	5.44E+14	±0.50%	5.01E+14	±0.51%

12.4 Neutron Flux Analysis Values and % Error

The error for the fast and thermal flux values obtained over nine core positions was obtained directly from the Serpent output file and is presented in Table 12.4 and Table 12.5 as the percent error with a 2σ confidence interval.

Table 12.4: Percent error for the flux values in the HEU 94CIC model

Flux Trap	Fast		Thermal	
	Flux	Error [%]	Flux	Error [%]
NW	3.94E+18	1.03	1.28E+18	1.95
SW	7.60E+17	1.31	6.95E+17	1.88
NE	2.10E+18	0.91	2.04E+18	1.26
SE	7.31E+17	1.28	6.60E+17	1.91
C	1.85E+18	0.79	1.55E+18	1.17
W	8.38E+17	1.21	8.17E+17	1.79
E	3.48E+17	1.30	1.93E+17	1.65
N	7.73E+17	1.25	7.57E+17	1.84
S	3.21E+17	1.33	1.75E+17	1.68

Table 12.5: Percent error for the flux values for 35/20 TRIGA[®] Model 1

Flux Trap	Fast		Thermal	
	Flux	Error [%]	Flux	Error [%]
NW	3.32E+18	0.85	1.14E+18	1.52
SW	6.66E+17	1.07	6.13E+17	1.56
NE	1.84E+18	0.73	1.86E+18	0.91
SE	6.52E+17	1.03	6.09E+17	1.47
C	1.51E+18	0.62	1.32E+18	0.89
W	6.96E+17	0.99	7.06E+17	1.45
E	2.98E+17	1.06	1.71E+17	1.20
N	6.40E+17	1.05	6.42E+17	1.48
S	2.78E+17	1.05	1.60E+17	1.26

12.5 Corner Lobe Power Error Analysis

The error, σ , for each of the lobe power values was calculated using equation 12.3, where n is the number of fuel elements associated with that lobe and σ_n is the error for each element power, at a 2σ confidence interval.

$$\sigma_{power} = \sqrt{\sigma_1^2 + \sigma_2^2 + \dots + \sigma_n^2} \quad 12.3$$

Table 12.6: 35/20 TRIGA[®] Model 1 lobe power values and percent error

Burnup [MWd]	NE		SE		SW		NW	
	Power [W]	Error [%]						
0.00E+00	2.03E+07	0.39	2.48E+07	0.36	2.49E+07	0.36	2.25E+07	0.38
1.20E+00	1.99E+07	0.40	2.48E+07	0.36	2.56E+07	0.35	2.23E+07	0.37
8.40E+02	2.01E+07	0.39	2.47E+07	0.36	2.49E+07	0.35	2.24E+07	0.37
1.68E+03	2.04E+07	0.39	2.45E+07	0.36	2.46E+07	0.36	2.20E+07	0.38
2.52E+03	2.00E+07	0.39	2.40E+07	0.36	2.41E+07	0.36	2.20E+07	0.38
3.36E+03	1.99E+07	0.39	2.37E+07	0.35	2.38E+07	0.34	2.13E+07	0.37
4.20E+03	1.95E+07	0.39	2.32E+07	0.35	2.32E+07	0.35	2.09E+07	0.38
5.04E+03	1.94E+07	0.38	2.29E+07	0.35	2.33E+07	0.35	2.13E+07	0.36
5.88E+03	1.94E+07	0.40	2.31E+07	0.35	2.34E+07	0.36	2.09E+07	0.37

Table 12.7: HEU lobe power values and percent error

Burnup [MWd]	NE		SE		SW		NW	
	Power [W]	Error [%]						
0.00E+00	1.99E+07	1.03	2.36E+07	0.93	2.34E+07	0.93	2.11E+07	0.97
1.20E+00	1.94E+07	1.02	2.35E+07	0.94	2.35E+07	0.93	2.12E+07	1.01
8.40E+02	2.02E+07	1.03	2.30E+07	0.95	2.33E+07	0.94	2.12E+07	0.95
1.68E+03	1.96E+07	1.07	2.31E+07	0.97	2.35E+07	0.96	2.14E+07	0.99
2.52E+03	1.96E+07	1.02	2.32E+07	0.97	2.33E+07	0.95	2.18E+07	1.00
3.36E+03	1.95E+07	1.03	2.36E+07	0.98	2.32E+07	0.96	2.13E+07	1.01
4.20E+03	1.92E+07	1.02	2.31E+07	0.97	2.34E+07	0.96	2.17E+07	0.98
5.04E+03	1.94E+07	1.06	2.44E+07	0.94	2.32E+07	0.97	2.12E+07	1.01
5.88E+03	1.95E+07	1.04	2.34E+07	0.96	2.32E+07	0.93	2.18E+07	1.00

12.6 Pin Power Values and Percent Error

The individual pin power values and the percent error, reported at a 2σ confidence interval, for each value is presented in Table 12.8.

Table 12.8: Pin power values and percent error for 35/20 TRIGA[®] Model 1

Pin #	Element 1		Element 2		Element 3		Element 4		Element 5	
	Power [W]	Error [%]								
1	2.21E+05	2.67	2.06E+05	2.62	1.44E+05	3.31	1.20E+05	3.71	1.07E+05	3.98
2	1.91E+05	2.78	1.79E+05	2.98	1.35E+05	3.40	1.06E+05	4.02	9.85E+04	4.13
3	1.95E+05	2.63	1.75E+05	2.91	1.44E+05	3.41	1.15E+05	3.74	9.94E+04	4.01
4	2.13E+05	2.69	1.98E+05	2.85	1.80E+05	3.03	1.32E+05	3.56	1.18E+05	3.81
5	1.95E+05	2.98	1.79E+05	3.00	1.19E+05	3.54	8.42E+04	4.40	7.23E+04	4.74
6	1.60E+05	3.17	1.45E+05	3.24	1.04E+05	3.84	7.19E+04	4.58	6.64E+04	4.67
7	1.54E+05	2.94	1.37E+05	3.20	1.04E+05	3.69	7.33E+04	4.40	6.53E+04	5.01
8	1.50E+05	3.12	1.41E+05	3.34	1.20E+05	3.44	8.07E+04	4.45	6.64E+04	4.87
9	1.84E+05	2.77	1.61E+05	3.12	1.50E+05	3.15	1.05E+05	3.93	8.18E+04	4.62
10	1.98E+05	2.86	1.75E+05	2.91	1.16E+05	3.77	7.38E+04	4.47	6.46E+04	4.87
11	1.60E+05	2.88	1.42E+05	3.28	1.04E+05	3.68	6.40E+04	4.69	5.47E+04	5.16
12	1.50E+05	3.28	1.36E+05	3.25	1.08E+05	3.58	6.44E+04	4.83	5.28E+04	4.94
13	1.49E+05	3.11	1.36E+05	3.17	1.14E+05	3.52	6.89E+04	4.53	5.11E+04	5.29
14	1.53E+05	3.24	1.41E+05	3.47	1.26E+05	3.30	7.43E+04	4.82	5.72E+04	5.11
15	1.78E+05	2.89	1.62E+05	3.08	1.62E+05	3.06	9.78E+04	4.31	7.02E+04	4.63
16	2.40E+05	2.56	1.79E+05	3.01	1.32E+05	3.84	7.55E+04	4.65	6.46E+04	5.25
17	2.08E+05	2.81	1.70E+05	2.91	1.36E+05	3.36	6.84E+04	4.75	5.48E+04	5.84
18	1.87E+05	2.89	1.77E+05	3.11	1.52E+05	3.35	6.96E+04	4.76	5.36E+04	6.19
19	1.73E+05	3.09	1.81E+05	2.99	1.65E+05	3.18	7.01E+04	5.14	5.03E+04	5.74
20	1.64E+05	3.03	1.88E+05	3.02	1.82E+05	3.08	7.89E+04	4.51	5.92E+04	5.43
21	1.75E+05	3.01	2.04E+05	2.90	2.04E+05	2.90	1.00E+05	4.10	6.93E+04	4.90

The error for the axial and radial power factors was found by finding the error (σ) in the average by first using equation 12.4 and then equation 12.5, where s is the number of segments in the distribution.

$$\sigma_{sum} = \sqrt{\sigma_1^2 + \sigma_2^2 + \sigma_3^2 + \dots} \quad 12.4$$

$$\sigma_{average} = \frac{\sigma_{sum}}{s} \quad 12.5$$

The error, σ_{PF} , in the power factor, PF , is found by propagating the error of the average, $\sigma_{average}$, and the error of the power, σ_P , using equation 12.6, where P is power.

$$\sigma_{PF} = PF \sqrt{\left(\frac{\sigma_P}{P}\right)^2 + \left(\frac{\sigma_{average}}{Average}\right)^2} \quad 12.6$$

The power factor and the relative error for the axial and radial power distributions are tabulated in

Table 12.9: Axial power factors and percent error for 35/20 TRIGA[®] Model 1

Axial Segment [cm]	Power Factor	Error [%]
0	4.53E-01	7.09
6.096	5.50E-01	5.96
12.192	7.45E-01	5.85
18.288	9.48E-01	4.97
24.384	1.03E+00	4.61
30.48	1.19E+00	4.14
36.576	1.34E+00	4.08
42.672	1.36E+00	4.05
48.768	1.40E+00	4.27
54.864	1.41E+00	3.98
60.96	1.39E+00	4.20
67.056	1.38E+00	4.23
73.152	1.32E+00	4.10
79.248	1.21E+00	4.39
85.344	1.10E+00	4.62
91.44	9.45E-01	4.90
97.536	8.37E-01	4.97
103.63	6.35E-01	5.85
109.72	4.57E-01	6.88
115.82	3.05E-01	8.72

Table 12.10: Radial power factors and percent error for 35/20 TRIGA[®] Model 1

Radial Position [cm]	Power Factor	Error [%]
0.00	9.46E-01	6.72
0.06	9.69E-01	3.99
0.11	9.40E-01	3.31
0.17	9.58E-01	2.86
0.23	9.65E-01	2.68
0.29	9.84E-01	2.41
0.34	1.01E+00	2.23
0.40	1.04E+00	2.02
0.46	1.08E+00	1.99
0.52	1.12E+00	1.87

12.7 Effective Delayed Neutron Fraction and Mean Neutron Generation Time

Table 12.11: Eff. delayed neutron fraction and mean neutron generation time error

Burnup [MWd]	HEU		Model 1		HEU		Model 1	
	β_{eff}	Error [%]	β_{eff}	Error [%]	Λ	Error [%]	Λ	Error [%]
0	7.20E-03	4.85	7.01E-03	1.82	7.35E-05	0.59	6.96E-05	0.27
1.2	6.98E-03	4.69	7.01E-03	1.85	7.34E-05	0.61	6.95E-05	0.27
840	7.12E-03	4.30	7.11E-03	1.71	7.32E-05	0.63	7.19E-05	0.27
1680	6.84E-03	4.86	6.98E-03	1.77	7.39E-05	0.66	7.19E-05	0.27
2520	7.30E-03	4.63	6.94E-03	1.69	7.46E-05	0.62	7.18E-05	0.26
3360	6.94E-03	4.65	6.89E-03	1.77	7.53E-05	0.64	7.13E-05	0.25
4200	7.18E-03	4.46	6.98E-03	1.76	7.57E-05	0.59	7.10E-05	0.26
5040	6.69E-03	4.93	6.82E-03	1.74	7.67E-05	0.64	7.19E-05	0.26
5880	7.01E-03	4.83	6.86E-03	1.74	7.71E-05	0.59	7.28E-05	0.25
6720	7.01E-03	4.70	6.89E-03	1.77	7.73E-05	0.60	7.35E-05	0.24

